ACS Catalysis

pubs.acs.org/acscatalysis

Research Article

Combined In Situ X-ray Powder Diffractometry/Raman Spectroscopy of Iron Carbide and Carbon Species Evolution in Fe(−Na−S)/α-Al_2O_3 Catalysts during Fischer−Tropsch Synthesis

Pasi P. Paalanen, Sophie H. van Vreeswijk, and Bert M. Weckhuysen*

Cite This: *ACS Catal.* 2020, 10, 9837−9855

Read Online

ACCESS | Metrics & More | Article Recommendations | Supporting Information

ABSTRACT: A Na−S promoted Fe-based Fischer−Tropsch synthesis (FTS) catalyst converts a H_2/CO gas mixture into hydrocarbons with enriched C_2−C_4 olefin content. Above 300 °C, the carbon-depositing Boudouard reaction competes with the FTS reaction for CO as reactant. By making use of a combined in situ X-ray powder diffractometry (XRPD)/Raman spectroscopy setup, the simultaneous evolution of the Fe_xO_y/α-Fe/Fe_xC phases and various formed carbon species has been monitored at 340 °C and 10 bar. CO carburized, Na−S promoted and unpromoted Fe(−Na−S)/α-Al_2O_3 catalysts were investigated. The various Fe phases present were quantified with Rietveld quantitative phase analysis (R-QPA) from the in situ collected XRPD patterns. The observed D- and G-bands in the in situ Raman spectra were analyzed for their relative intensities, band widths, and positions and compared to reference carbon materials. It was found that amorphous carbon with C sp^3 and C sp^2 in chain-like ordering evolved toward carbon nanofiber-like structures during FTS. Na−S promotion and initial CO carburization at temperatures ≥340 °C led to an increased amount of cyclic sixfold C sp^2 species. Preliminary carbon deposits present in the catalysts decreased the initial fast increase of the Raman band intensities, while Na−S promotion increased Raman band intensity growth after the initial fast increase period. The carbon species evolution was unaffected by the presence of specific Fe carbides or by carbide-to-carbide transitions. Na−S promotion aided in the reduction of Fe_3O_4 by (H_2:)CO to carbon-depositing Fe carbides. The results obtained add to our further understanding on the role of Fe and carbon species during a high-temperature FTS reaction.

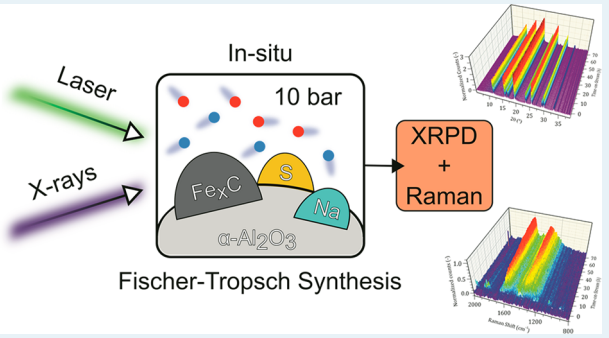

KEYWORDS: *heterogeneous catalysis, Fischer−Tropsch synthesis, iron carbides, Na−S promotion, X-ray powder diffractometry, Rietveld quantitative phase analysis*

INTRODUCTION

With the Fischer−Tropsch synthesis (FTS) reaction, a H_2/CO gas mixture can be converted into valuable hydrocarbons.[1−11] With the combination of a high reaction temperature (320−375 °C), an Fe-based catalyst, and Na−S chemical promotion, the synthesized hydrocarbon product slate can be directed toward the formation of valuable, short-chained (C_2−C_4) olefins.[12−22] However, for reaction temperatures ≳300 °C,[2,23−25] the Boudouard reaction (i.e., CO disproportionation of CO into C and CO_2) also becomes active, depositing carbon material onto the catalytically active phase. The Boudouard reaction therefore competes with the FTS directly for the reactant CO.[26,27] Regeneration and removal of the carbon deposits would be possible via catalyst hydrogenation at temperatures ≥350 °C.[2] However, because of the (possible) fragmentation of the catalyst material due to carbon deposition, especially with bulk Fe catalysts, the catalyst's lost mechanical stability cannot be remedied with simple hydrogenation treatments.[2,28−30]

Under FTS reaction conditions, Fe-based catalysts form various (near-)zerovalent Fe carbides.[19] The Fe carbides are the CO dissociating active phases necessary for both the competing FTS and Boudouard reactions.[19,27,31,32] Deposition of inactive carbon has been proposed to be associated with the presence of θ-Fe_3C (cementite)[33−35] and/or to the transition of C-rich "ε-carbides" (i.e., η-Fe_2C in more precise nomenclature) to lesser C-containing χ-Fe_5C_2 (the Hägg carbide) or θ-Fe_3C.[36−39]

Chemical elements from the alkali metal group, most often Na or K, are commonly added as promoters to Fe-based FTS catalyst materials. These alkali promoters intrinsically increase the carbon deposition rate.[2,23] In contrast, S as promoter is commonly observed to decrease the overall carbon deposition on Fe-based catalysts.[40−44] However, the addition of S also

Received: April 25, 2020
Revised: July 28, 2020
Published: August 19, 2020

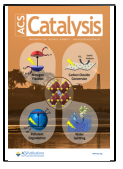

https://dx.doi.org/10.1021/acscatal.0c01851
ACS Catal. 2020, 10, 9837−9855

results in an overall decreased CO conversion, therefore necessarily decreasing the carbon deposition.[45] Decreased CO conversion can also lead to the removal of reactor bed hotspots, which as well can lead to the observations of decreased carbon deposition.[46−49] In other words, the addition of S does not necessarily alter the C selectivity between the FTS and Boudouard reactions,[49] unlike alkali promoters. When Na and S are added together as promoters, the combined Na−S promotion behaves "alkali-like", and the carbon deposition is effectively increased in high-temperature FTS in comparison to unpromoted catalyst materials.[17,20,39]

The type of carbon formed, deactivating the FTS catalyst, is often described with loosely defined terms, such as "graphitic-like"[34,38,50,51] or as an amorphous carbonaceous overlayer.[51−53] Furthermore, the formation of fibrous carbon species is possible under FTS reaction conditions, in the presence of H_2 or other hydrogen-containing chemical species.[37,54−56] The formation of carbon species has been proposed to be related to the transition of C-rich ("η") into C-poor (χ, θ) Fe carbide phases. It has been proposed that the C atoms, ejected from the Fe carbide lattice, function as the nucleation centers for the deactivating carbon formation.[36−38] The carbon species are thought to evolve from initial polymeric carbon toward more ordered carbon structures.[38,51]

X-ray powder diffractometry (XRPD) is a suitable tool for characterizing the Fe carbide phases and is also widely applied in the field of FTS catalysis.[5,25,29,33,34,36,57−61] Raman spectroscopy is a technique capable for differentiating between "graphitic-like", amorphous, and fibrous carbon species[62−66] but is much less used to characterize FTS catalyst materials.[67−78] Both characterization methods can in principle also be applied under in situ or operando conditions, thereby allowing probing of the changes in the Fe phases and carbon deposit formation during the FTS reaction. Previously, such an in situ/operando Raman spectroscopy approach has been applied, e.g., to follow the formation of carbon deposits during the catalytic dehydrogenation of light alkanes[79,80] and the Co-based FTS reaction.[81]

In this work, we combine XRPD and Raman spectroscopy in one experimental setup for studying the transformation of the different Fe phases as well as the evolution of carbon species under in situ conditions. This is done with a setup recently developed in our research group.[81] The catalysts under study are characterized under FTS reaction conditions of 340 °C at 10 bar in a H_2/CO 2:1 gas mixture. The studied catalyst materials are supported Fe(−Na−S)/α-Al_2O_3 catalysts, prepared with and without Na−S promotion. The catalysts have been prepared to contain preformed Fe carbides (i.e., ε-Fe_3C, η-Fe_2C, χ-Fe_5C_2, and/or θ-Fe_3C) via a CO carburization step or to contain α-Fe/Fe_xO_y phases via a H_2 reduction step.[39] Rietveld quantitative phase analysis (R-QPA) is used to quantify the collected in situ XRPD data. The R-QPA derived Fe phase content changes and the Fe phases' crystallite diameters are qualitatively compared to changes observed in the simultaneously collected in situ Raman spectra.

EXPERIMENTAL SECTION

Catalyst Preparation. Details on the catalyst synthesis and applied catalyst treatments of CO carburization and H_2 reduction are described in detail in reference [39]. In short, nominal 7 wt % of Fe on α-alumina (BASF, 7 m^2/g, 212−425 μm particle size) supported (Fe-(Na−S)/α-Al_2O_3) catalysts, with or without Na−S promotion, were synthesized with the use of incipient wetness impregnation. Nominal promoter loadings of 0.29 wt % for Na and 0.04 wt % for S were used.

Ammonium Fe(III) citrate (Acros, 211840010) was used as the Fe precursor, Fe(II) sulfate heptahydrate (Sigma-Aldrich, 215422) was used as the S precursor, and Na tribasic citrate dihydrate (Sigma-Aldrich, S4641) was used as the Na precursor.

The synthesized catalyst materials were calcined under dry air flow at 500 °C for 6 h, reduced under H_2/N_2 flow at 400 °C for 5 h, and cooled down to 200 °C under the H_2/N_2 flow. The H_2 reduced catalyst materials were subsequently carburized with CO without removing the catalyst from the reactor. Under the set H_2/N_2 flow, the reduced catalyst was heated up (10 °C/min) from 200 °C to a desired carburization temperature. Upon reaching the desired carburization temperature, the H_2/N_2 flow was switched to pure CO flow. The carburization temperatures and times used were 240 °C (2 h), 340 °C (16 h), and 440 °C (16 h). After the desired carburization period, the CO flow was switched to pure N_2, and the reactor was cooled down to room temperature and flushed with N_2 for several hours. The impurities in the N_2 gas are sufficient to passivate the Fe surfaces without a need for a dedicated O_2 passivation step. Further details of this can be found from reference [39]. H_2 reduced catalysts used for the experiments were prepared identically to the carburized ones but without the CO carburization step.

Linde Gas Benelux supplied all the gases used in catalyst preparation, i.e., H_2, N_2 (both grade 5.0, i.e., 99.999% pure), CO (grade 2.5, i.e., 99.5% pure), and dry, compressed air. Table 1 summarizes the shorthand notation applied within this work to identify the different catalysts under study.

Table 1. Overview of the Used Shorthand Notation for Catalyst Materials under Study

shorthand notation	catalyst material description
H_2	H_2 reduction at 400 °C for 5 h, after the calcining step
240, 340, 440	CO carburization (at 1 atm) temperature in °C, after the reduction step
UP	unpromoted Fe/α-Al_2O_3 catalyst
Na−S	Na−S promoted Fe−Na−S/α-Al_2O_3 catalyst
Carb.	catalyst material after H_2 reduction or CO carburization ("fresh catalyst")
Q-FTS	catalyst material after 72 h, 340 °C, 10 bar in situ FTS run, measured quasi-in-situ at 100 °C (0.5 bar, 1:1 Ar/He) ("spent catalyst")

Catalyst Characterization. *Details of In Situ Reactor Cell.* The (ex situ) prepared catalyst materials were characterized under FTS reaction conditions using a modified iKey in situ XRPD plug flow capillary reactor cell from Cape Catalytix.[82−84] The cell was combined with a high-temperature Raman spectroscopy probe.[81] The iKey reactor cell unit employs two infrared (IR) heater blocks for heating the reactor capillary up to the reaction temperature (Figure S1). The reaction temperature is measured with a thermocouple inserted inside the reactor capillary. The original reactor cell was modified by reversing the inlet for reactant gas flow in order to avoid hydrocarbon condensation on the thermocouple inserted inside the reactor capillary. In addition, the IR heaters were covered with a custom-made stainless steel "chimney" in order to decrease the thermal radiance from the IR heater blocks that is seen by the Raman probe. Furthermore, the IR heater blocks were resistance matched in order to acquire a uniform isothermal heating zone.

https://dx.doi.org/10.1021/acscatal.0c01851
ACS Catal. 2020, 10, 9837−9855

Reactor cell temperature calibration was performed under a nominal input flow of 1 mL/min of Ar and 1 mL/min of He by moving the thermocouple inside the reactor capillary while keeping the power fed to the heater at set constant. The reactor isothermal zone was measured to be 340 ± 1.4 °C over a distance of ∼11.0 mm. Further details on the used reactor cell type and the laboratory-based XRPD/Raman spectroscopy setup can be found from the literature.[81−83,85−87]

Catalytic Reaction. The catalyst materials were inserted to 1000 μm (10 μm wall thickness) borosilicate capillaries. An undiluted catalyst bed of ∼11 mm (6.4−7.2 mg of catalyst material with a 212−425 μm catalyst particle size), pinned in between quartz wool plugs, was used for each separate in situ FTS reaction run. Prior to each run, the experimental setup was leak tested at 100 °C under 1:1 Ar/He (2 mL/min) flow with the loaded sample capillary in place. After the leak test, the capillary reactor pressure was set to 0.5 bar(g). The FTS reactions were performed at 340 °C, at 10 bar of total pressure of H_2/CO/He (2.0:1.0:0.33 volume ratio). The nominal input gas flows to the in situ reactor were 0.6 mL/min of H_2, 0.3 mL/min of CO, and 0.1 mL/min of He, giving a gas hourly space velocity (GHSV, as total input gas flow per total reactor bed volume) of ∼7200 h^{-1}. After the initial leak testing at 100 °C, the reactor capillary was heated to 120 °C (10 °C/min) and pressurized at 120 °C to 10 bar of total reaction pressure. The pressurizing was done with 5× the FTS reaction gas flows, within 1 h. After reaching the 10 bar reaction pressure, the reactor was heated to the reaction temperature of 340 °C (2 °C/min). The 0 h time-on-stream (ToS) was taken as the moment when 340 °C was reached, and the FTS reaction was then subsequently ran for 72 h. After the 72 h FTS reaction, the reactor was cooled down to 100 °C within 1 h under the set H_2/CO/He flow, while the reaction pressure was simultaneously decreased to 0.5 bar(g) (0.5 bar/min). At 100 °C, the input gas flow was switched to 1:1 Ar/He (2 mL/min), and the reactor was flushed under the inert gases. H_2, Ar, and He gas purities were grade 5.0, and the CO gas purity was grade 2.5, as supplied by Linde Gas Benelux. During the FTS reactions, up- and downstream pressure gauges and a mass flow meter upstream of the reactor capillary were used to follow possible mass flow limitations in the reactor bed. No mass flow limitations were observed in any of the performed FTS reaction runs.

In Situ X-ray Powder Diffractometry. In situ X-ray powder diffractometry (XRPD) patterns were collected during the FTS reaction (340 °C, 10 bar, H_2/CO/He) as well as in quasi-in-situ (at 100 °C, 0.5 bar, Ar/He, i.e., "spent catalyst") after the respective 72 h FTS reaction run (shorthand Q-FTS). The initial "fresh catalyst" (shorthand Carb.) was measured also under 100 °C (0.5 bar, Ar/He) after the initial leak testing step. For collecting the in situ XRPD patterns, a Bruker D8 Discover diffractometer instrument in Debye−Scherrer transmission (capillary) geometry with a Mo (Kα1 0.709 Å) source was used. At the beginning of each in situ reaction run, the capillary was moved to the focus of the X-ray beam (beam ≈ 600 × 15 000 μm, height × width) for maximum diffraction. The X-ray diffraction patterns were collected over a 2θ range of 5−39° with a scan step size of 0.015°. For collecting the X-ray diffraction patterns before and after the FTS reaction (quasi-in-situ), 6 h of total measurement time was used. For the in situ measurements during the FTS reaction at 340 °C and during the pressurizing and temperature ramp steps, 0.5 h of total measurement time was used.

The R-QPA method was employed for quantifying the crystalline Fe phases from the collected XRPD patterns. The application of R-QPA fitting has been described in detail in reference [39] and is applied here in a similar manner, with few modifications in the applied fitting model. As the primary modification, the lattice parameters for the support material α-Al_2O_3 were also refined simultaneously with the rest of the fitted phases. This was done in order to accommodate the thermal expansion of the material's lattice during the in situ measurements at elevated temperature. The effects of crystal lattice thermal expansion,[88] reactor capillary deformation/displacement, and sample material density changes in the capillary[89] all affect the phases' diffraction peak positions and thus the lattice parameters observed in the performed in situ XRPD measurements. The changes to the lattice parameters for the fitted phases could not be decoupled from the mentioned experimental effects in the in situ XRPD runs, and the intrinsic phase lattice parameters could not be solved for the fitted phases. All refined lattice parameters were constrained to an arbitrary range with constraints from −0.01 to +0.05 Å from their literature values.[39] The R-QPA fitting models and constraint values were adjusted until the measured XRPD diffraction peak positions were satisfactorily accounted for. The literature and database sources for the crystal structures used in the R-QPA fitting models are given in reference [39].

As further differences to the previously applied fitting model, all measured XRPD pattern backgrounds were modeled with a third order Chebyshev polynomial. Three independent Lorentzian peaks were used for fitting the amorphous content scattering and/or diffraction contribution within the range of ∼8−12° 2θ. Predetermined R-QPA fitting models were applied on the measured quasi- and in situ measured XRPD patterns over the full XRPD measurement range using a batch mode with the Bruker TOPAS v5.0 software. The phases with <0.4 wt % phase content and/or relative wt % fitting errors ≥30% were removed from the fitting models.

The measured, background subtracted XRPD patterns were aligned and normalized to the α-Al_2O_3 peak (0 2 4) at its nominal position of 23.515° 2θ (at Mo Kα1) at room temperature, for presenting the diffraction pattern heatmaps versus the FTS reaction ToS. The R-QPA derived values from the in situ XRPD runs are reported as five-point median values of the data points obtained every 0.5 h and expressed with the median's standard deviation (STD) as an error estimate. R-QPA derived values for the "fresh catalysts" and quasi-in-situ measured "spent catalysts" after the FTS reaction run are reported for each single (6 h) measurement with their respective R-QPA fitting errors as the error estimates.

In Situ Raman Spectroscopy. Simultaneously to the in situ XRPD measurements, in situ Raman spectroscopy measurements were performed in order to follow the formation and further evolution of carbon species within the catalysts during the FTS reactions. A thermoelectrically cooled AvaRaman (Avantes) spectroscopy system with a 50 mW 532 nm excitation laser coupled with a high-temperature InPhotonics Raman probe with an ∼200 μm measurement spot size at focus was used. The spectrometer's spectral resolution was 6 cm^{-1}.

At the start of each FTS reaction run, the Raman probe was focused on the catalyst bed using the α-Al_2O_3 peak at ∼4389 cm^{-1} (see, e.g., RRUFF database #R040096 for reference). The dark spectrum corrected in situ Raman spectra were collected over a spectral range of ∼174−5685 cm^{-1}. A single Raman spectrum was recorded every 10 min by averaging 600 scans

https://dx.doi.org/10.1021/acscatal.0c01851
ACS Catal. 2020, 10, 9837−9855

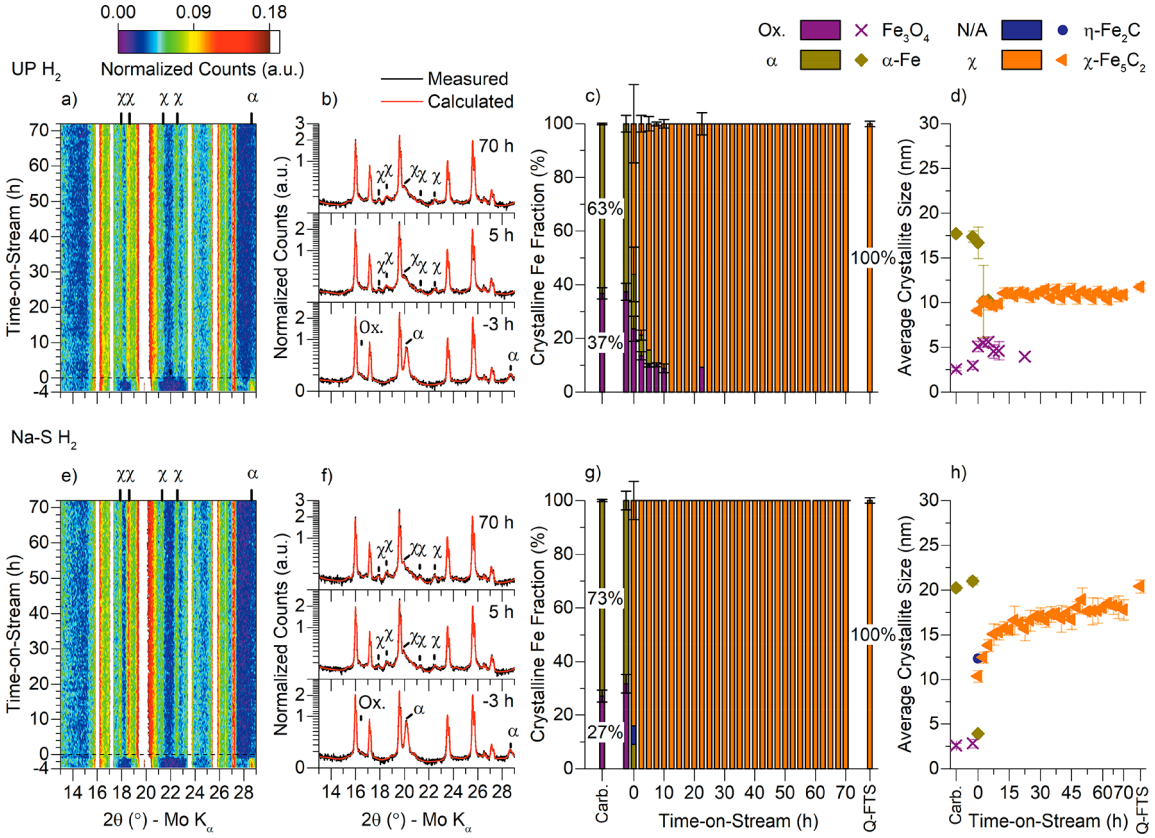

Figure 1. In situ X-ray powder diffractometry (XRPD) results of the UP (Fe/α-Al_2O_3) (top row) and Na−S H_2 (Fe−Na−S/α-Al_2O_3) (bottom row) catalysts during a 72 h Fischer−Tropsch synthesis (FTS). (a,e) Heatmaps of aligned and background corrected, in situ collected XRPD patterns, (b,f) measured and Rietveld method calculated XRPD patterns at −3, 5, and 70 h time-on-stream (ToS), (c,g) the crystalline Fe phase composition of the catalyst, and (d,h) Fe phases' average crystallite sizes during the 72 h FTS reaction. The measurements before (Carb.) and quasi-in-situ (Q-FTS) after the FTS reaction run are included for comparison. FTS conditions: 340 °C, 10 bar, H_2/CO/He = 2.0:1.0:0.33 v/v, ∼7200 h^{-1}.

with a 1 s integration time. Carbon nanofibers (CNF, Pyrograf, PR-24-XT-LHT), graphite (Aldrich, 282863), activated carbon (AC, Alfa Aesar, Norit ROW 0.8 mm, L16334) and carbon nanotubes (CNT, Baytubes, C150 HP) were measured as reference materials. The reference materials were measured at room temperature (600 scans with a 1 s integration time) using a standalone LaserQuantum MPC 6000 532 nm laser operated at 200 mW of power. The same AvaRaman spectrometer and the high-temperature InPhotonics Raman probe were used to collect the carbon reference spectra as was used for the in situ Raman Spectroscopy measurements.

The in situ collected Raman spectra were corrected for (fluorescence or thermal radiation) background with the use of the asymmetric least squares smoothing (ALSS) algorithm. The so-called D (∼1350 cm^{-1}) and G (∼1600 cm^{-1}) Raman bands were fitted with four peak shapes. An iterative peak fitting (Levenberg−Marquardt) algorithm was used to find the best fit to the measured spectra. The D-band was fitted with a Lorentzian peak D_1 at ∼1320 cm^{-1} and Gaussian peaks D_3 at ∼1500 cm^{-1} and D_4 at ∼1220 cm^{-1}. The G-band was fitted with a single Gaussian peak shape. The data points that had ≥40% relative error in the fitted peak area or width were filtered out. Peaks fitted for the D_3 and D_4 positions were constrained near their nominal locations during the iterative peak fitting process. This was done in order to avoid the tendency of the D_3 and D_4 peaks from shifting and nearly or fully overlapping with the D_1- and G-band positions. Thus, the D_3 peak was constrained to a range of 1465−1525 cm^{-1}, and D_4 was constrained to a range of 1100−1230 cm^{-1} during the fitting process. The obtained fitted peak positions were used to follow the D- and G-band peak position shifts during the FTS reaction. The peak intensities I(D) (D_1-band) and I(G) (G-band) in the measured in situ Raman spectra were obtained from the locations defined by the fitted peak positions as three-point median values. The fitted peak widths were used to estimate the measured D- and G-band widths as peak full width at half maximums (fwhms). The collected data points obtained every 10 min were averaged to 12-point median values and are presented with their corresponding STDs as the error estimates. For each in situ Raman measurement run, the obtained Raman spectra were normalized to the background corrected maximum peak intensity of the Raman G-band within 0−72 h ToS. The measured carbon reference materials were normalized to the background corrected maxima of their respective Raman G-bands and fitted with four individual peaks akin to the measured data.

RESULTS AND DISCUSSION

In Situ X-ray Powder Diffractometry. Figures 1−4 summarize the results for the different in situ XRPD reaction runs conducted for the Fe/α-Al_2O_3 (UP) and the Na−S promoted Fe−Na−S/α-Al_2O_3 (Na−S) catalyst materials with preformed Fe carbides (Table 1). The aligned and background corrected in situ collected XRPD patterns during the FTS reactions are given as heatmaps (Figures 1a−4a and 1e−4e) as well as individual diffraction patterns at the start of the FTS reaction at −3 h (120 °C, H_2/CO), 5 h, and 70 h ToS (340 °C,

https://dx.doi.org/10.1021/acscatal.0c01851
ACS Catal. 2020, 10, 9837−9855

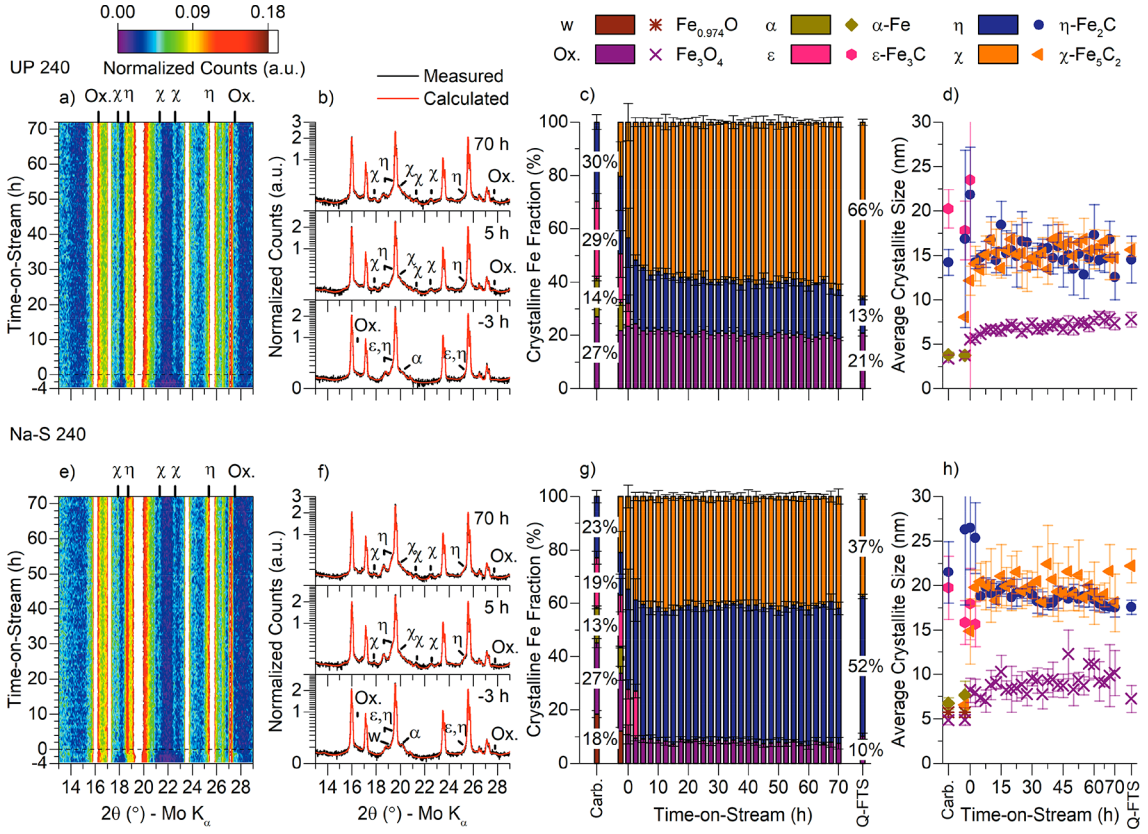

Figure 2. In situ X-ray powder diffractometry (XRPD) results of the UP (Fe/α-Al_2O_3) (top row) and Na−S 240 (Fe−Na−S/α-Al_2O_3) (bottom row) catalysts during a 72 h Fischer−Tropsch synthesis (FTS). (a,e) Heatmaps of aligned and background corrected, in situ collected XRPD patterns, (b,f) measured and Rietveld method calculated XRPD patterns at −3, 5, and 70 h time-on-stream (ToS), (c,g) the crystalline Fe phase composition of the catalyst, and (d,h) Fe phases' average crystallite sizes during the 72 h FTS reaction. The measurements before (Carb.) and quasi-in-situ (Q-FTS) after the FTS reaction run are included for comparison. FTS conditions: 340 °C, 10 bar, H_2/CO/He = 2.0:1.0:0.33 v/v, ∼7200 h^{-1}.

H_2/CO) (Figures 1b−4b and 1f−4f). Markers for the characteristic Fe phase diffraction positions have been added to the figures with X-ray diffraction patterns.[39]

For each of the measured individual diffraction patterns, the corresponding Rietveld method calculated patterns are also included in the figures (Figures 1b−4b and 1f−4f). The most intense and sharp diffraction peaks in the individual diffraction patterns in the figures (e.g., at 19.58 and 27.13° 2θ) originate from the support α-Al_2O_3, a phase of which diffraction markers are excluded for convenience.

The Fe carbide phases observed in the FTS reaction related research have been previously identified as ε-Fe_3C $P6_322$ (182), η-Fe_2C *Pnnm* (58), χ-Fe_5C_2 *C*2/*c* (15) (the Hägg carbide), θ-Fe_3C *Pnma* (62) (cementite), and θ-Fe_7C_3 *Pnma* (62) (Eckström−Adcock carbide).[39,90] For all of the performed Rietveld method fittings (i.e., R-QPA) on the quasi- and in situ measured XRPD patterns, the previously identified Fe carbide crystal structures give very good calculated fits (Figures 1b−4b and 1f−4f). Despite the Fe oxide phase being fitted with a Fe_3O_4 crystal structure, similar overall R-QPA fits could have been archived with ferrihydrite crystal structures.[91] The Rietveld method calculated Fe phase patterns have been given and discussed in detail in reference [39] and are for brevity omitted here.

Quantitative Analysis of the Fe Phases. For both UP and Na−S H_2 catalysts, upon reaching the 0 h ToS as well as the FTS reaction temperature of 340 °C, the majority of the initially present α-Fe/Fe_xO_y phases transform into the temperature's most stable Fe carbide phase of χ-Fe_5C_2 (Figure 1c,g).[29,36,92−99] Without the added Na−S promotion, the transition of α-Fe/Fe_xO_y phases into χ-Fe_5C_2 takes longer in comparison to the promoted catalysts. At 0 h ToS, for the Na−S H_2 catalyst, the χ-Fe_5C_2 phase already accounts for ∼81 ± 7% of the Fe phases (Figure 1g), while for the UP H_2 catalyst, only ∼56 ± 15% of the χ-Fe_5C_2 phase is present (Figure 1c).

This observation can be explained by the alkali effect, i.e., Na(−S) promotion helps the reduction of Fe oxides at ≲300 °C by CO.[39,60,100,101] In the Na−S H_2 catalysts, the Fe oxidation shell is removed more efficiently by CO in the presence of Na(−S) promotion during the temperature ramp (∼−2−0 h ToS) to 340 °C than with the unpromoted UP H_2 catalysts. The Fe oxides, which are present as an Fe particle shell and/or core, are reduced into α-Fe and subsequently converted into the χ-Fe_5C_2 phase by CO. Regardless of the Na−S promotion, the transition of α-Fe into Fe carbides in the presence of CO at temperatures ≳200−250 °C is very fast[36,98,102−104] and not the limiting step in the Fe carbide formation.[105]

When comparing the UP and Na−S 240 catalyst materials with the initial presence of the ε-Fe_3C and η-Fe_2C phases in the Carb. catalyst materials, the presence of Na−S promotion stabilizes the η-Fe_2C phase during the FTS reaction run. For the Na−S 240 Q-FTS measurement, 50 ± 1% of the η-Fe_2C phase is quantified (Figure 2g) after the FTS reaction run in comparison to 13 ± 1% of the phase in UP 240 Q-FTS catalyst material (Figure 2c).

https://dx.doi.org/10.1021/acscatal.0c01851
ACS Catal. 2020, 10, 9837−9855

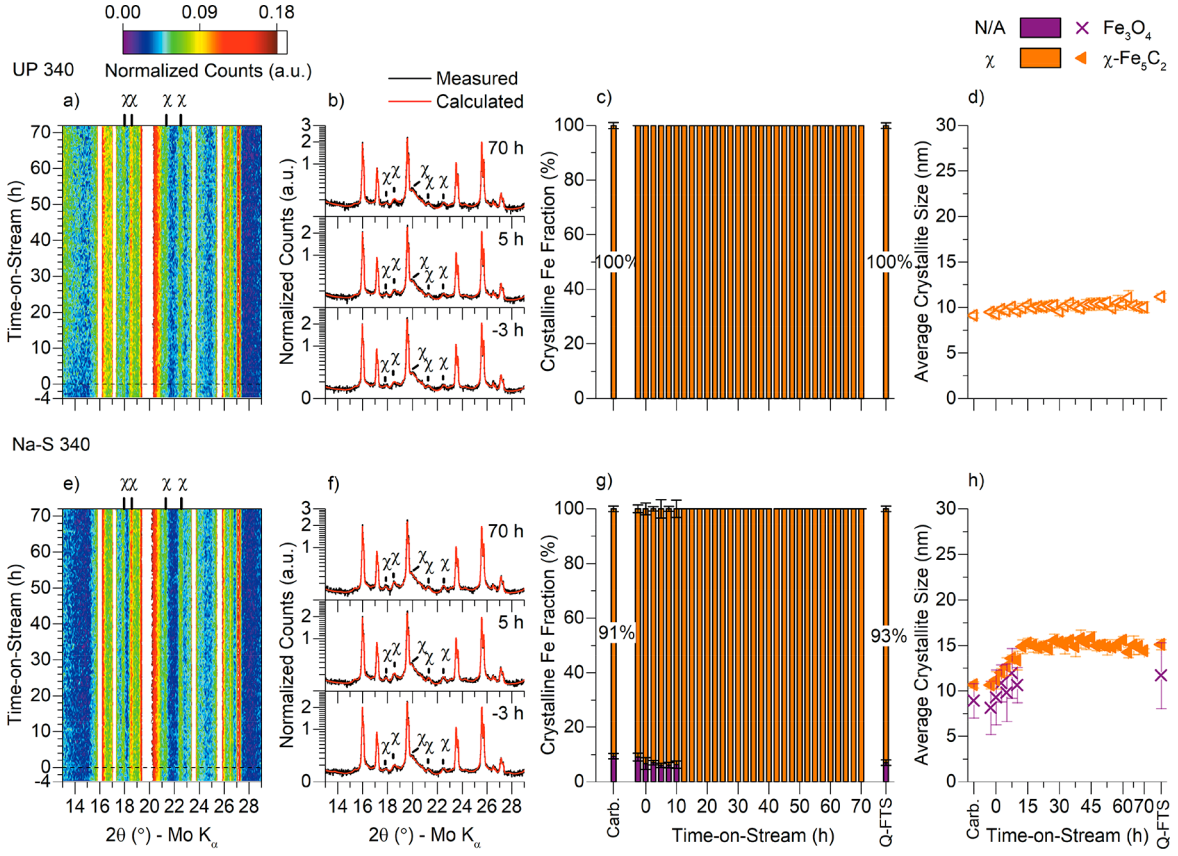

Figure 3. In situ X-ray powder diffractometry (XRPD) results of the UP (Fe/α-Al_2O_3) (top row) and Na−S 340 (Fe−Na−S/α-Al_2O_3) (bottom row) catalysts during a 72 h Fischer−Tropsch synthesis (FTS). (a,e) Heatmaps of aligned and background corrected, in situ collected XRPD patterns, (b,f) measured and Rietveld method calculated XRPD patterns at −3, 5, and 70 h time-on-stream (ToS), (c,g) the crystalline Fe phase composition of the catalyst, and (d,h) Fe phases' average crystallite sizes during the 72 h FTS reaction. The measurements before (Carb.) and quasi-in-situ (Q-FTS) after the FTS reaction run are included for comparison. FTS conditions: 340 °C, 10 bar, H_2/CO/He = 2.0:1.0:0.33 v/v, ∼7200 h^{-1}.

The relative amount of "ε-carbides" (i.e., ε-Fe_3C/η-Fe_2C phases) is generally increased in Fe-based FTS catalysts after the FTS reaction with added alkali elements as K or Na.[5,60,106,107] Furthermore, the η-Fe_2C phase does not form ≳300 °C, *but* it can be stable up to ∼340 °C if it has formed and is present prior to the FTS reaction,[39] as is the case here. Thus, the results for the H_2 and 240 catalyst materials show an observable Na(−S) stabilization effect of the preformed η-Fe_2C phase in the 340 °C FTS reaction. Without Na(−S) promotion, a significantly lesser amount of the initial ε-Fe_3C/η-Fe_2C phases are stabilized as the η-Fe_2C phase during the high-temperature FTS reaction.

The exact physical origin on the alkali-induced stability of the η-Fe_2C phase is unclear and not devisible from the current data. It can be speculated that the stabilization effect could be due to alkali preventing expulsion of the C atoms from the η-Fe_2C phase's lattice, thus hindering its transition to less C atoms containing χ-Fe_5C_2 phase.[39] This would be analogous to increased stability of the θ-Fe_3C phase against decomposition to α-Fe and C, if an oxidation layer covers the carbide preventing C atom expulsion.[39]

Interestingly, the requirement for the a priori presence of the ε-Fe_3C/η-Fe_2C phases for the stability of the η-Fe_2C phase in the FTS reaction is comparable to the stability behavior of "ε-iron (carbo)nitrides".[108] These Fe (carbo-)nitrides have crystal structures closely related to the ε-Fe_3C/η-Fe_2C phases.[109−114] The precise, fundamental reasons for the increased stability behavior with the added Na(−S) promotion in the FTS reaction with crystal structures corresponding to the η-Fe_2C and "ε-iron (carbo)nitrides" phases would make an interesting topic for a further study.

Besides the stabilization of the η-Fe_2C phase by the Na−S promotion addition in the Na−S 240 catalyst materials, the catalysts' Fe_3O_4 content is also reduced during the FTS reaction. A steady Fe_3O_4 fraction of ∼20% is quantified for the UP 240 catalyst (Figure 2c), while for the Na−S 240 catalyst material (Figure 2g), only ∼8% of Fe_3O_4 is observed after the start of the FTS reaction. This difference in the Fe oxide content is visible (at ∼27.5° 2θ) in the in situ collected XRPD patterns (Figure 2a,e). The added alkali has been observed to reduce the Fe oxide content in Fe-based FTS catalysts during the reaction also in the literature,[106,107] in agreement with the results for the Na−S 240 catalyst material. In contrast to this, Na−S promotion increases the Fe oxide content in the Na−S 240 Carb. catalysts after the CO carburization (i.e., in the fresh catalysts), as is evident by comparing the R-QPA quantifications in Figure 2c,g. This effect presumably originates from the Na−S promotion-induced increase on Fe phase affinity toward O atoms from the CO dissociation during the CO carburization step with a short treatment time and temperature.[39]

Despite the Na−S 240 catalyst behaving as expected, i.e., Na−S promotion decreasing the content of Fe_3O_4 during FTS, it is difficult to understand why both UP and Na−S 240 catalysts show the presence of Fe_3O_4 *at all* during the in situ XRPD runs. Any of the UP H_2, 340 or 440 (Figures 1c, 3c, and 4c), or Na−S H_2, 340 or 440 (Figures 1g, 3g, and 4g) catalysts *do not* show a significant presence or stabilization of the Fe_3O_4 phase. Perhaps,

https://dx.doi.org/10.1021/acscatal.0c01851
ACS Catal. 2020, 10, 9837−9855

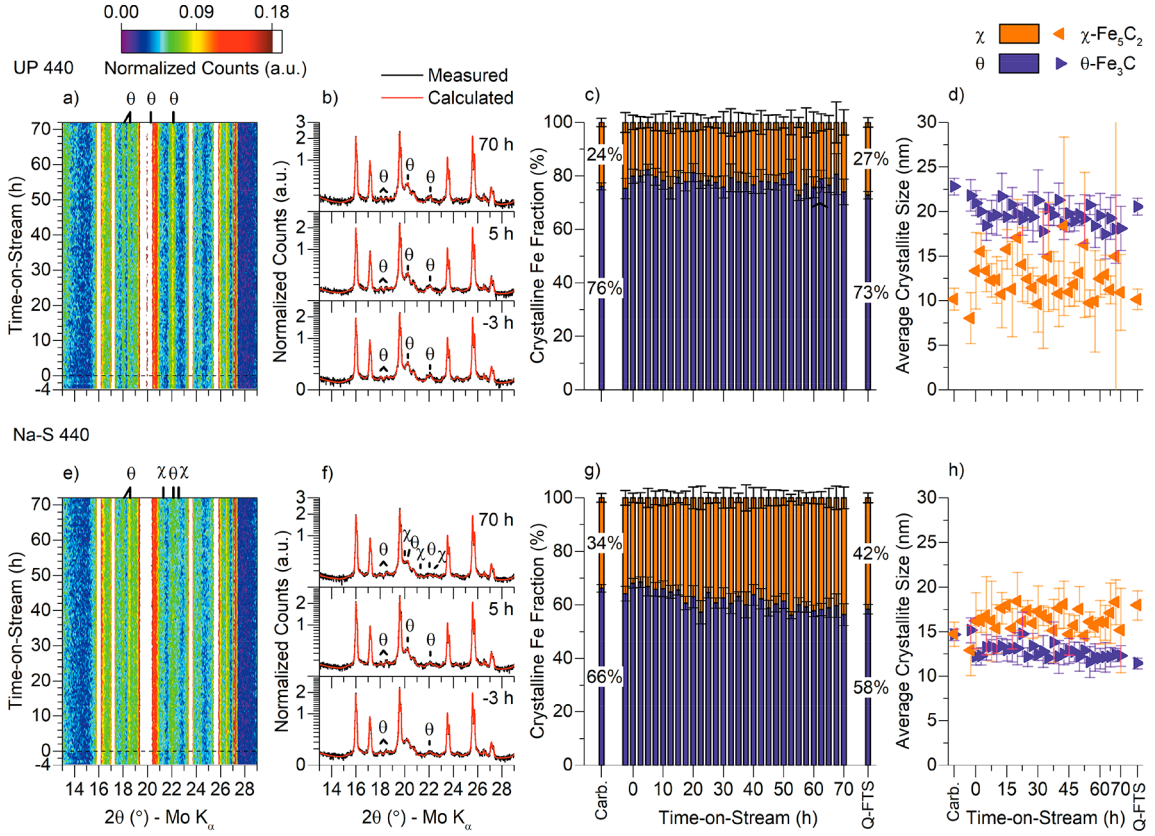

Figure 4. In situ X-ray powder diffractometry (XRPD) results of the UP (Fe/α-Al_2O_3) (top row) and Na−S 440 (Fe−Na−S/α-Al_2O_3) (bottom row) catalysts during a 72 h Fischer−Tropsch synthesis (FTS). (a,e) Heatmaps of aligned and background corrected, in situ collected XRPD patterns, (b,f) measured and Rietveld method calculated XRPD patterns at −3, 5, and 70 h time-on-stream (ToS), (c,g) the crystalline Fe phase composition of the catalyst, and (d,h) Fe phases' average crystallite sizes during the 72 h FTS reaction. The measurements before (Carb.) and quasi-in-situ (Q-FTS) after the FTS reaction run are included for comparison. FTS conditions: 340 °C, 10 bar, H_2/CO/He = 2.0:1.0:0.33 v/v, ∼7200 h^{-1}.

the ε-Fe_3C/η-Fe_2C phases might be more susceptible toward reoxidation by CO_2 and H_2O[2,29,115−117] than the other Fe carbide phases are.

With respect to the phase changes in the UP and Na−S 340 and 440 catalyst materials during their respective FTS reaction runs, only minor changes take place in contrast to the initial Carb. catalyst materials (Figures 3c,g and 4c,g). A small amount of Fe_3O_4 (∼7%) is present in the Na−S 340 catalyst during the first 10 h ToS of the FTS reaction. For the UP 340 catalyst material, no presence of Fe oxide is quantified. In comparison to UP 340, the promoted Na−S 340 catalyst is expected to have a higher CO conversion resulting in higher H_2O and CO_2 concentrations in the reactor.[90] Reoxidation by the H_2O and/or CO_2 might explain the minor Fe oxide content in the Na−S 340 catalyst during the FTS run (Figure 3g).[90] Finally, for the UP and Na−S 440 catalyst materials, the effect of Na−S promotion is to aid the transformation of the θ-Fe_3C phase into χ-Fe_5C_2, which is the most stable Fe carbide at 340 °C,[39] during the FTS reaction (Figure 4c,g). With the Na−S 440 catalyst material, the θ-Fe_3C phase content steadily decreases with increasing χ-Fe_5C_2 contribution (Figure 4g).

Changes in the Crystallite Diameters of the Fe Phases. The in situ XRPD observations for the R-QPA derived Fe phases' crystallite (volume-weighted) mean diameters follow the Fe phase quantities in the FTS reaction. The increasing phase quantity in general translates to increasing Fe phase crystallite diameters, as more of the phase is present, thus allowing the formation of larger crystallites. The Fe crystallite diameter evolutions are plotted in Figures 1d−4d and 1h−4h for the different catalysts under study.

Additionally, the presence of Na−S promotion favors the formation of larger Fe carbide crystallites for the H_2, 240, and 340 catalysts, while for the 440 catalyst, the situation is mixed. The Na−S H_2, 240, and 340 catalyst materials show Fe carbide crystallite growth within the first ∼10 h ToS in comparison to their UP catalyst counterparts (Figures 1d−3d and 1h−3h). This could be associated with Fe particle growth, which has been observed to take place within the first hours of the FTS reaction when Na−S promotion is added to the catalyst.[20] However, *Fe crystallite growth does not necessitate Fe particle growth*, as the measurables are different.[118] Thus, definitive conclusions whether Fe particle growth takes place cannot be made solely on the basis of the in situ XRPD derived R-QPA crystallite diameter results. Whatever the fundamental origins are, the Na−S promotion causes increased Fe carbide crystallite mean diameters, and the increase takes place within the first ∼10 h ToS of the FTS reaction.

The peculiar effect of Na−S promotion decreasing the θ-Fe_3C phase's stability is also observed in the changes of the θ-Fe_3C phase's crystallite diameters between the UP and Na−S 440 catalyst materials (Figure 4d,h). The added Na−S promotion induces a slow decrease to the θ-Fe_3C crystallite mean diameters over the reaction ToS, while both the χ-Fe_5C_2 content (Figure 4g) and its crystallite mean diameter increase simultaneously (Figure 4h).

https://dx.doi.org/10.1021/acscatal.0c01851
ACS Catal. 2020, 10, 9837−9855

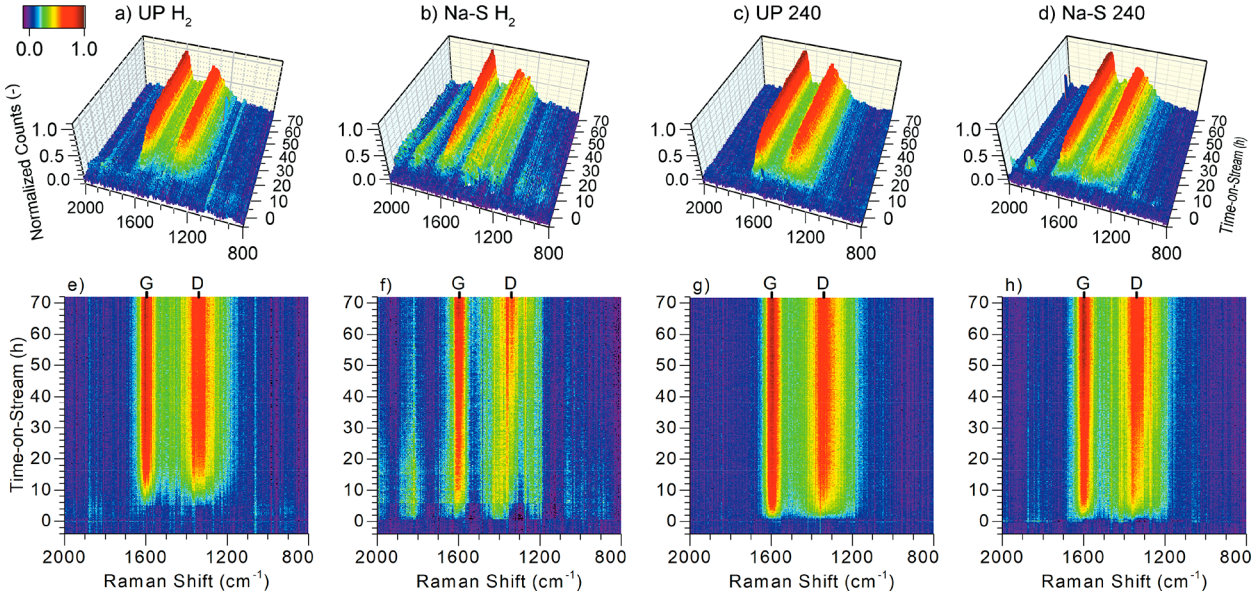

Figure 5. In situ Raman spectroscopy results of the H_2 and 240 catalysts during a 72 h Fischer−Tropsch synthesis (FTS). 3D plot of background corrected and normalized Raman spectra (top row) and corresponding heatmaps (bottom row) for (a,e) UP H_2; (b,f) Na−S H_2; (c,g) UP 240; and (d,h) Na−S 240 (Fe(−Na−S)/α-Al_2O_3) catalysts. D- (∼1350 cm^{-1}) and G-bands (∼1600 cm^{-1}) are marked in the heatmaps (D,G). FTS conditions: 340 °C, 10 bar, H_2/CO/He = 2.0:1.0:0.33 v/v, ∼7200 h^{-1}.

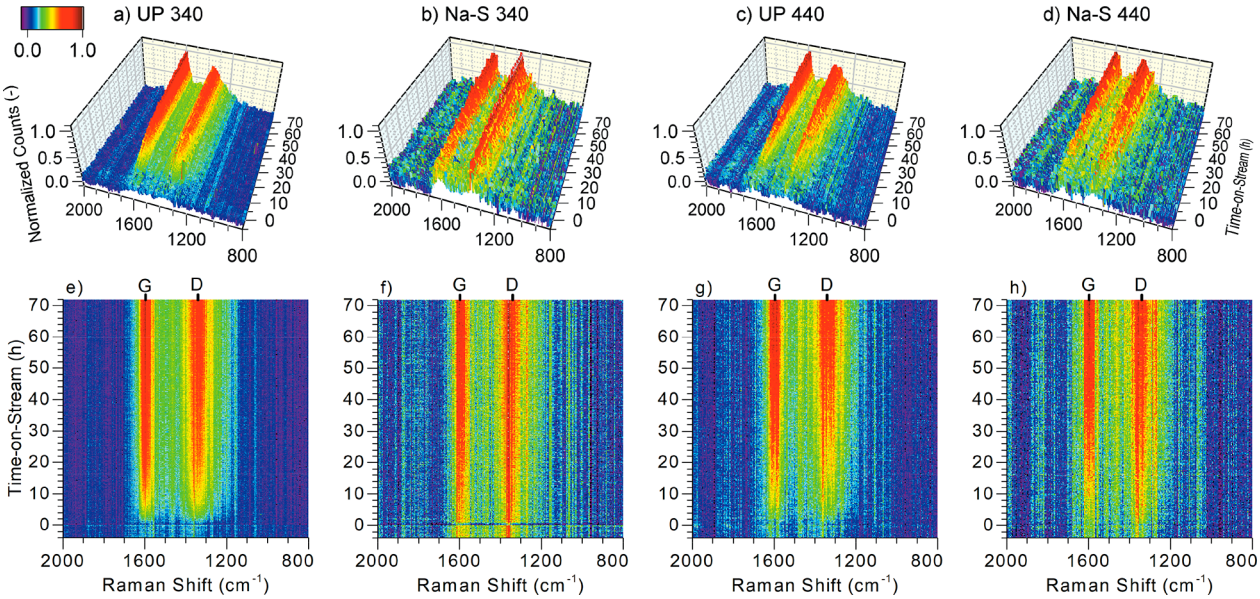

Figure 6. In situ Raman spectroscopy results of the 340 and 440 catalysts during a 72 h Fischer−Tropsch synthesis (FTS). 3D plot of background corrected and normalized Raman spectra (top row) and corresponding heatmaps (bottom row) for (a,e) UP 340; (b,f) Na−S 340; (c,g) UP 440, and (d,h) Na−S 440 (Fe(−Na−S)/α-Al_2O_3) catalysts. D- (∼1350 cm^{-1}) and G-bands (∼1600 cm^{-1}) are marked to the heatmaps (D,G). FTS conditions: 340 °C, 10 bar, H_2/CO/He = 2.0:1.0:0.33 v/v, ∼7200 h^{-1}.

Furthermore, the large crystallite mean diameters with large STDs for the ε-Fe_3C and η-Fe_2C phases at ∼0 h ToS are due to correlations between the ε-Fe_3C, η-Fe_2C, and α-Al_2O_3 lattice parameters. During the temperature ramp $\lesssim$0 h ToS, the ε-Fe_3C and η-Fe_2C crystal structures tend to fit to the sharp α-Al_2O_3 diffraction peak (1 1 3) at ∼19.58° 2θ, giving rise to very large crystallite mean diameters with large STDs. After the steady FTS reaction temperature is reached and/or the ε-Fe_3C phase is consumed $\gtrsim$3 h ToS, no correlation exists anymore with the η-Fe_2C and α-Al_2O_3 phases, and η-Fe_2C crystallite mean diameters become consistent again (Figure 2d,h).

Summarizing the above-described results, the Na−S promotion has the following effects

(i) to stabilize the η-Fe_2C phase *if* ε-Fe_3C and/or η-Fe_2C phases are present in the initial catalyst at the start of the FTS reaction (Na−S H_2 versus Na−S 240);

(ii) to decrease the Fe_3O_4 content (UP 240 versus Na−S 240);

(iii) to destabilize θ-Fe_3C phase during the FTS reaction (UP 440 versus Na−S 440); and

(iv) the Fe carbide crystallite mean diameters grow larger within the first 10 h ToS (excluding the θ-Fe_3C in Na−S

https://dx.doi.org/10.1021/acscatal.0c01851
ACS Catal. 2020, 10, 9837−9855

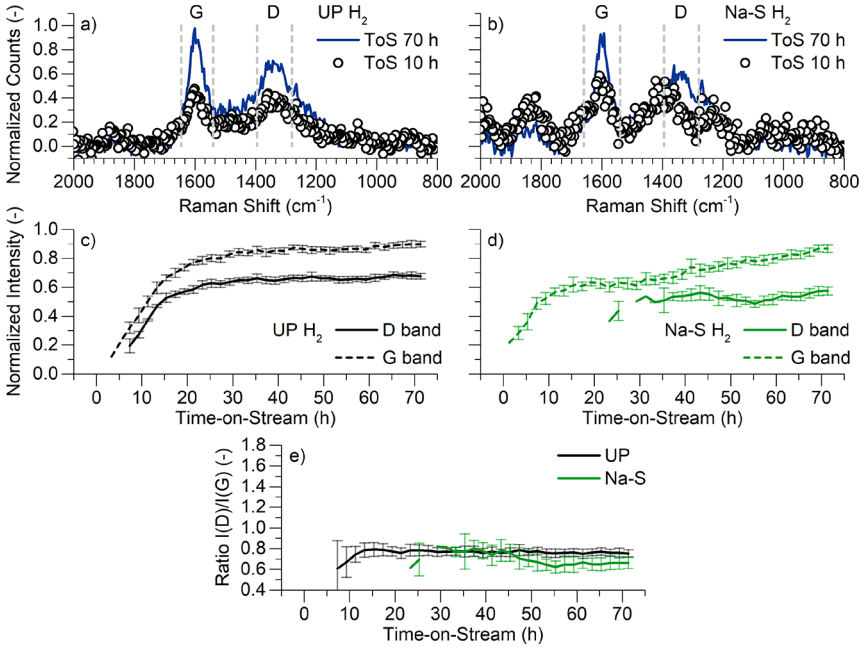

Figure 7. Analysis of changes in the D- and G-band intensities as derived from the in situ collected Raman spectra of the H_2 catalysts during a 72 h Fischer−Tropsch synthesis (FTS). Comparison of background corrected and normalized Raman spectra at 10 and 70 h time-on-stream (ToS) for (a) UP H_2 and (b) Na−S H_2 (Fe(−Na−S)/α-Al_2O_3) catalysts. Gray vertical dashed lines mark the Raman D- (∼1350 cm^{-1}) and G-band (∼1600 cm^{-1}) regions. Changes in the intensities of the G- and D-bands for (c) UP H_2 and d) Na−S H_2 and the bands' intensity ratio $I(D)/I(G)$ for (e) UP and Na−S H_2 catalysts during the 72 h FTS reaction.

440 catalyst material) in comparison to the respective UP catalysts.

In Situ Raman Spectroscopy. *Raman Spectroscopy of Carbon Deposits during Fischer−Tropsch Synthesis.* Simultaneously to the in situ XRPD data collection, in situ Raman spectroscopy measurements were performed over the duration of the 72 h FTS reactions. With FTS reaction temperatures above ∼300 °C, the Boudouard reaction deposits carbon from CO on the FTS reaction catalyst materials.[2,23−25] In the spectra, bands with Raman shifts of ∼1350 cm^{-1} (D-band) and ∼1600 cm^{-1} (G-band) can be found, which originate from carbon species.[62−66,119] These bands can be used to follow the carbon deposition process over the course of the FTS reaction. The in situ collected, background corrected, and normalized Raman spectra of the studied catalyst materials are given as 3D plots and heatmaps in Figures 5 and 6. The in situ Raman spectra are shown over the Raman shift range of 800−2000 cm^{-1} showing the evolution of the D- and G-bands during the 72 h ToS in the FTS reaction.

The deviations in the in situ collected Raman spectra for the Na−S H_2 catalyst material (Figure 5b,f), in comparison to other Raman measurements (e.g., UP 240, Figure 5c,g), originate from a very high fluorescence or thermal radiance background during the FTS reaction run. This complicated the background correction for the in situ Raman spectra collected for the Na−S H_2 catalyst, creating artifacts to the spectra with a period of ∼198 ± 6 cm^{-1}.

The in situ collected Raman spectroscopy data are not quantitative without a proper use of an internal standard. Inherently, the intensity of the Raman spectra is dependent on the focus of the incident excitation laser on the catalyst as well as on the color (i.e., the relative fraction of absorbed and scattered light) of the catalyst material, thereby causing variations in the absolute amount of scattered photons collected by the detector. Thus, the quantity of the deposited carbon is not directly comparable based on the Raman measurements between the different FTS reaction runs in this study. In addition, any carbon species present in the Carb. catalyst materials at the beginning of the FTS reaction runs decreased the collected Raman D- and G-band intensities. During the catalyst preparation, the Na−S 340 Carb. as well as the UP and Na−S 440 Carb. catalysts deposit carbon during the CO carburization step.[39] This can be deduced from the in overall decreased non-normalized Raman band intensities (data not shown for brevity) and thus as decreased signal-to-noise ratios in the normalized Raman spectra, as seen in Figure 6b−d,f−h. On the counts per second (CPS) scale with the background corrected data, the highest G-band intensity was collected for the Na−S 240 (∼0.055 CPS) and the lowest for the Na−S 440 (∼0.023 CPS) catalyst material.

Notwithstanding the above considerations, a qualitative discussion on the collected in situ Raman spectra is possible by normalizing the observed Raman intensities to the maximum of, for example, the G-band within each respective FTS reaction run. By following the relative band intensity ratio $I(D)/I(G)$ and the spectral positions for the D- and G-bands, information on the type and ToS dependent evolution of the carbon species can be followed over the course of the FTS reaction.[65]

The observable Raman shifts with the visible wavelength (i.e., 532 nm) laser excitation originate from differences in the polarizability of the π-bonding in the carbon-containing compounds. Long-range polarizable C sp^2 π-bonds give rise to the Raman D- and G-bands, while C sp^3 σ-bonds polarize poorly, being weakly or non-Raman active with a visible light wavelength excitation laser.[65] The G-band is assigned to cyclic and/or chain structures with C sp^2, while the D-band originates from the presence of disorder/defects in the cyclic C sp^2 arrangements.[62,64−66] The differences in the C sp^2 and C sp^3 bond polarization and thus in the observed Raman signal intensity are also another reason why quantification of the

https://dx.doi.org/10.1021/acscatal.0c01851
ACS Catal. 2020, 10, 9837−9855

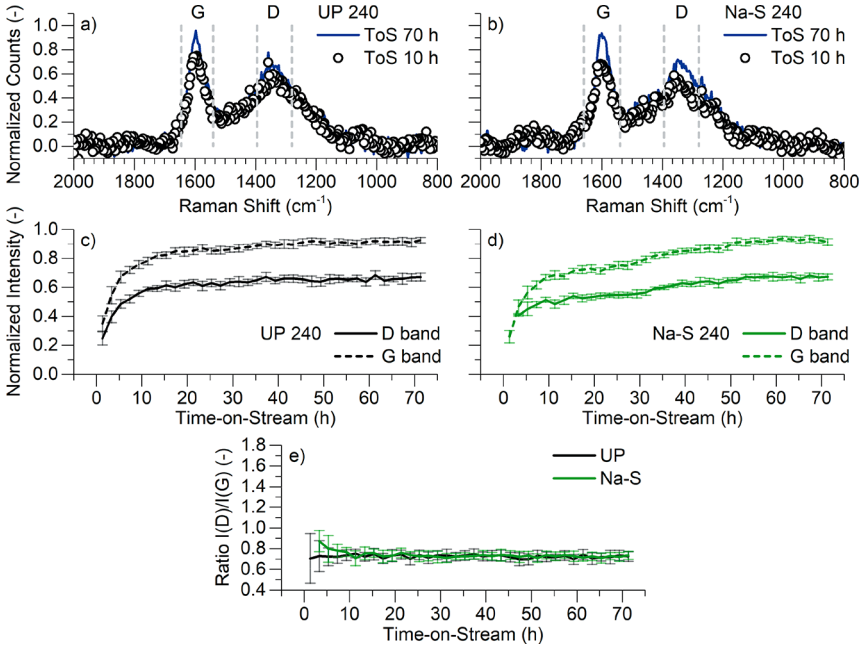

Figure 8. Analysis of changes in the D- and G-band intensities as derived from in situ collected Raman spectra of the 240 catalysts during a 72 h Fischer−Tropsch synthesis (FTS). Comparison of background corrected and normalized Raman spectra at 10 and 70 h time-on-stream (ToS) for (a) UP 240 and (b) Na−S 240 (Fe(−Na−S)/α-Al_2O_3) catalysts. Gray vertical dashed lines mark the Raman D- (∼1350 cm^{-1}) and G-band (∼1600 cm^{-1}) regions. Changes in the intensity of the G- and D-bands for (c) UP 240 and (d) Na−S 240 and the bands' intensity ratio I(D)/I(G) for (e) UP and Na−S H_2 240 catalysts during the 72 h FTS reaction.

deposited carbon species during the FTS reaction is hard to determine with in situ Raman spectroscopy.

Nevertheless, both the D- and G-bands are present in all the recorded in situ Raman spectra, as shown in Figures 5 and 6. This points toward formation of C sp^2-containing carbon species with disordered structures,[66] within the different FTS reaction runs, and requires further analysis and discussion.

Changes in the D- and G-Band Intensities and Their Positions. Figures 7−10 summarize the evolution of the intensities of the D- and G-bands, as determined from the collected in situ Raman spectra versus the FTS reaction ToS. The corresponding, measured I(D)/I(G) band intensity ratios are also included in these figures.

First, an interesting yet expected difference can be observed between the UP and Na−S H_2 catalysts on how their D- and G-band intensities develop as a function of the FTS reaction ToS. With the UP H_2 catalyst, the initial D- and G-bands only appear after an onset period of ∼5−7 h ToS, while with the Na−S H_2 catalyst, the G-band appears at ∼0 h ToS (Figure 7c,d). This behavior matches with the in situ XRPD results. As the carbon-depositing Boudouard reaction requires CO dissociation (i.e., CO disproportionation to C and CO_2),[26,27] the Fe_3O_4 phase needs to be converted first into (near-)zerovalent Fe carbides capable of dissociating CO.[19,31,120] Without Na−S promotion, the conversion of the Fe_3O_4 phase into the χ-Fe_5C_2 phase is slower under H_2/CO conditions (Figure 1c,g), resulting in the onset period for the appearance of the D- and G-bands for the UP H_2 catalyst (Figure 7c). This effect also explains literature observations of the lower initial deposition of carbon with unpromoted Fe-based catalysts with respect to Na−S promoted catalysts.[20] However, it is worth to keep in mind the earlier mentioned background-induced spectral deviations in the Raman spectra of the Na−S H_2 catalyst, which may skew the results. This especially true for the early FTS reaction ToS.

For the UP and Na−S 240, 340, and 440 catalysts, no significant differences in the G- and D-band appearance onset times are observed (Figures 8c−10c and 8d−10d). The majority of these phases within the catalysts are Fe carbides at the start of the FTS reactions, carbides that are capable of CO dissociation (Figures 2c−4c and 2g−4g).

With respect to the different Fe crystalline phases: the C atoms ejected during the transition of C-rich "ε-carbides" (i.e., η-Fe_2C),[39] to the lesser C-containing Fe carbides (χ, θ) have been proposed to act as nucleation sites for carbon formation.[36−38] As has been experimentally shown in reference [39] for the Fe carbides observable in the FTS reaction, the η-Fe_2C phase is C-rich, while the ε-Fe_3C phase contains the least number of C atoms in the carbides' crystal lattices. Thus, the transition of the η-Fe_2C phase into χ-Fe_5C_2 or θ-Fe_3C phases should correlate to changes in the Raman spectra. However, no direct correlation exists between any of the Fe carbide phases or carbide-to-carbide transitions observed in the in situ XRPD (Figures 1c−4c and 1g−4g) and the simultaneous in situ Raman D- and G-band intensity evolutions (Figures 7c−10c and 7d−10d).

The changes in the D- and G-band intensities derived from the collected in situ Raman spectra have two regions of band intensity growth for the UP and Na−S H_2 and 240 catalysts (Figures 7c,d and 8c,d). These can be divided into two categories: (i) within ∼10−15 h ToS from the initial appearance of the D- and G-bands, the intensity growth is fast, and (ii) after ≥20 h ToS, the D- and G-band intensities settle to near steady values or to a lower rate of intensity growth. With the Na−S H_2 catalysts, the initial D- and G-band intensity growth is observed to be lesser , which is, possibly, due to data analysis problems instigated by the high background. However, with Na−S promotion, the D- and G-band intensities continue growing after the initial fast growth period (≲15 h ToS), unlike with the UP H_2 and 240 catalysts. The normalized, median G-band intensity increases with a rate of ∼4.7 ± 0.3 × 10^{-3} h^{-1} for the

https://dx.doi.org/10.1021/acscatal.0c01851
ACS Catal. 2020, 10, 9837−9855

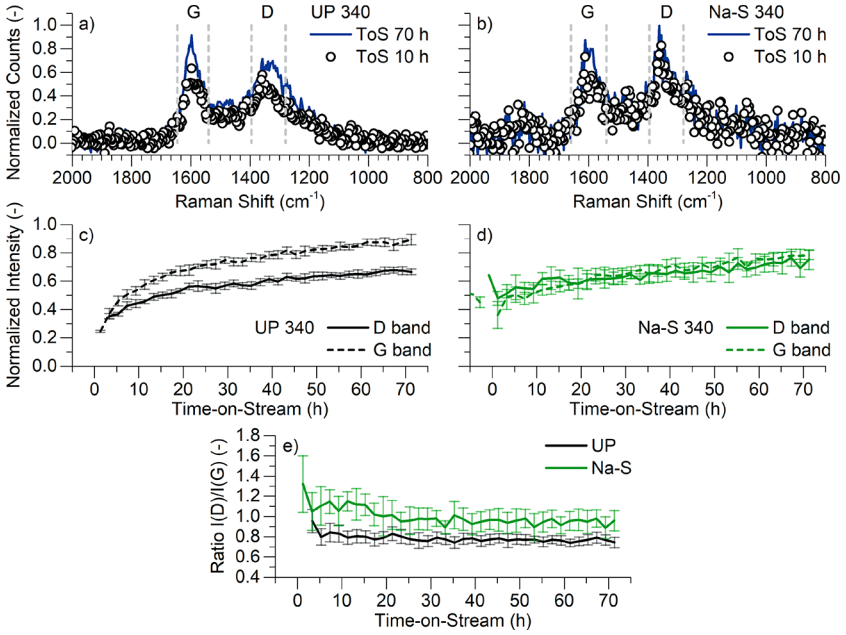

Figure 9. Analysis of changes in D- and G-band intensities as derived from in situ collected Raman spectra of the 340 catalysts during a 72 h Fischer−Tropsch synthesis (FTS). Comparison of background corrected and normalized Raman spectra at 10 and 70 h time-on-stream (ToS) for (a) UP 340 and (b) Na−S 340 (Fe(−Na−S)/α-Al_2O_3) catalyst materials. Gray vertical dashed lines mark the Raman D- (∼1350 cm^{-1}) and G-band (∼1600 cm^{-1}) regions. Changes in the intensity of the G- and D-bands for (c) UP 340 and (d) Na−S 340 and the bands' intensity ratio I(D)/I(G) for (e) UP and Na−S H_2 340 catalysts during the 72 h FTS reaction.

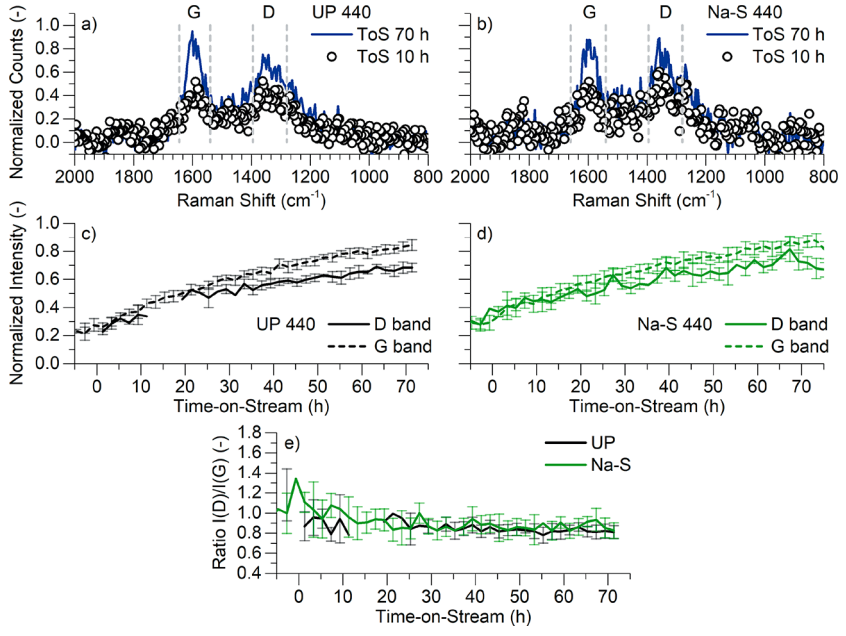

Figure 10. Analysis of changes in D- and G-band intensities as derived from in situ collected Raman spectra of the 440 catalysts during a 72 h Fischer−Tropsch synthesis (FTS). Comparison of background corrected and normalized Raman spectra at 10 and 70 h time-on-stream (ToS) for (a) UP 440 and (b) Na−S 440 (Fe(−Na−S)/α-Al_2O_3) catalyst materials. Gray vertical dashed lines mark the Raman D- (∼1350 cm^{-1}) and G-band (∼1600 cm^{-1}) regions. Changes in the intensities of the G- and D-bands for (c) UP 440 and (d) Na−S 440 and the bands' intensity ratio I(D)/I(G) for (e) UP and Na−S H_2 440 catalysts during the 72 h FTS reaction.

Na−S H_2 and 240 and ∼1.9 ± 0.7 × 10^{-3} h^{-1} for the UP H_2 and 240 catalysts over the ∼21−70 h ToS period (Figure 7c,d and 8c,d). In other words, the G-band intensities grow ∼2.5 ± 0.9 faster for the Na−S than for the respective UP H_2 and 240 catalysts.

This can be expected as the Na−S catalysts can have significantly higher CO conversions than the UP catalysts under the FTS reaction conditions applied in this work.[13,20] This most probably leads to a higher rate of the Boudouard reaction.[26] The added alkali Na(−S) promotion also intrinsically increases the carbon deposition rate for the Fe-based catalysts.[2,39]

Nevertheless, the initial fast period (≲15 h ToS) of intensity growths of the D- and G-bands take place for both the UP and Na−S 240 catalysts regardless of the Na−S promotion. This

https://dx.doi.org/10.1021/acscatal.0c01851
ACS Catal. 2020, 10, 9837−9855

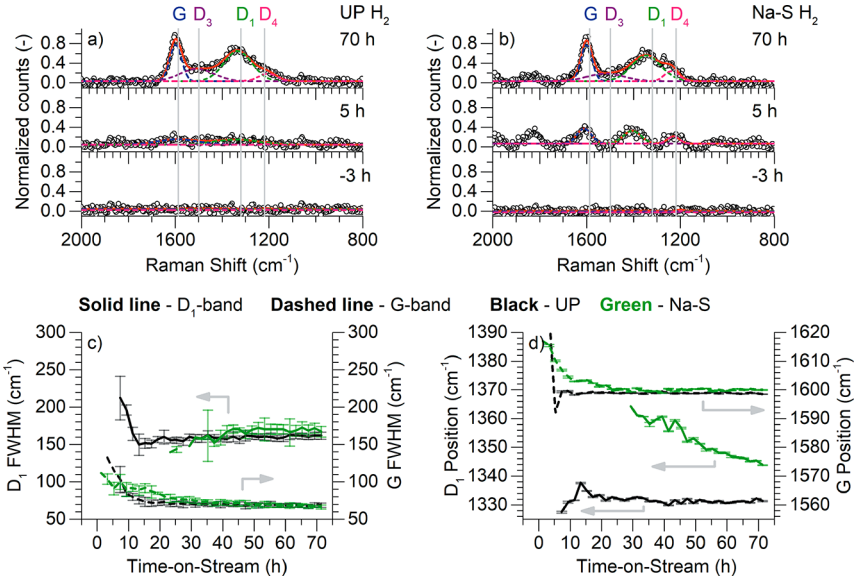

Figure 11. Peak fitting of the in situ collected Raman spectra of the H_2 catalysts during a 72 h Fischer−Tropsch synthesis (FTS). The measured Raman spectra at −3, 5, and 70 h time-on-stream (ToS) with fitted G, D_1, D_3, and D_4 peaks for (a) UP H_2 and (b) Na−S H_2 (Fe(−Na−S)/α-Al_2O_3) catalysts. Vertical gray lines mark the corresponding nominal Raman band positions, fitted peaks are indicated by their colored letters, and the cumulative fit is in red. The peak D_1- and G-band widths over 72 h ToS are in (e) and positions are in (d) for UP and Na−S H_2 catalysts.

suggests that non-Na−S promotion related phenomena are operative, perhaps such as the reactor bed heating by the exothermic FTS reaction.[121] A 10 °C increase in the reactor bed temperature in the FTS reaction can already increase the carbon deposition by ∼50%.[2]

Furthermore, similarly to the results in Figures 7c,d and 8c,8d, two-phase carbon deposition periods have been observed by Sancier, Isakson, and Wise.[122] The initial fast rate growth deposition period was proposed to be due to the initial Fe carburization, which however is not supported by our results. For example, the UP H_2 (as α-Fe/Fe_xO_y) and Na−S 240 (as ∼89% Fe carbides at ∼0 h ToS) catalysts (Figures 1c and 2g) behave in a similar manner with respect to their D- and G-band intensities (Figures 7c and 8d), regardless of their initial level of Fe carburization. For the UP and Na−S 340 and 440 catalysts, with initial carbon deposits present from the CO carburizations applied in the catalyst preparation,[39] the initial fast step ($\lesssim$15 h ToS) of rapid D- and G-band intensity growth is absent (Figures 9c,d and 10c,d). The UP 340 catalyst, with the least amount of initially deposited carbon within the group of UP and Na−S 340 and 440 catalysts, shows a slight yet subdued initial fast increase in Raman signal intensity. Thus, either the initial carbon deposits (i) dilute the catalyst bed with FTS inert carbon, allowing a more isothermal bed operation, (ii) cover and deactivate the supported Fe particles, i.e., decrease the CO conversion, and/or (iii) hide the Fe surface, where the Boudouard reaction takes place, from the Raman probe decreasing the observed Raman signal. That is, the Raman inactive carbon species formed during CO carburization should be different from the Raman active carbon species formed during the FTS reaction. The type of carbon species formed during the in situ reaction runs will be discussed more later on in the text.

All of the above listed phenomena would effectively decrease the observable Raman signal from the carbon deposition during the FTS reaction. However, which explanation is the most correct cannot be deduced from our results.

For all of the FTS reaction runs, the $I(D)/I(G)$ band intensity ratios are within the range of ∼1.0−0.7 (Figures 7e−10e). As exceptions, the Na−S 340 and 440 catalyst materials show initially higher >1.0 $I(D)/I(G)$ ratios (Figures 9e and 10e), due to poor data quality (Figure 6f,h). At a different measurement spot, the quasi-in-situ measured Raman spectrum and the $I(D)/I(G)$ ratio of the Na−S 340 catalyst were comparable to the other FTS reaction runs (Figure S4). Due to a hysteresis phenomenon, when carbon species evolve from tetrahedral C sp^3 toward C sp^2 carbon species with more order, the interpretation of the $I(D)/I(G)$ band intensity ratios is not straightforward.[65] Nevertheless, the measured Raman spectra with an $I(D)/I(G) < 1.0$ can be assigned to carbon species with little crystal order and/or disordered structures.[66] These structures/crystallites/clusters forming the individual carbon species particles have diameters < 7 nm.[66] The decrease in the $I(D)$ intensity (i.e., $I(D)/I(G) < 1.0$) and the increase in the D-band width, as will be discussed below, are both signs of the presence of cyclic C sp^2 carbon species that have cyclic carbon *different* from cyclic sixfold carbon structures. Increasing the $I(D)/I(G) \gtrsim 1.0$ ratio in turn signifies the increasing presence of clustered sixfold cyclic C sp^2 (i.e., aromatic) carbon structures,[65] in disordered carbon species.[65,66]

Deconvolution of the Raman Spectra. In a next step of our data analysis and following the approach by Sadezky et al.,[119] the Raman spectra can deconvoluted into a set of peaks, such as D_1 centered at ∼1320 cm^{-1}, D_2 at ∼1620 cm^{-1}, D_3 at ∼1500 cm^{-1}, and D_4 at ∼1220 cm^{-1}. The G-band at ∼1590 cm^{-1} is thought to correspond to the ring vibration of the defect-free graphitic lattice (E_{2g} symmetry). The D_1 position is believed to arise from disordered graphite lattice with A_{1g} symmetry (e.g., in graphene layer edges). The D_2 position in turn is assignable, e.g., to graphite disorder with E_{2g} symmetry in the graphene surface layers. The D_3 position is often associated with presence of amorphous carbon. Finally, the D_4 position signals the presence of a disordered graphitic lattice with A_{1g} symmetry (e.g., polyenes or ionic impurities).[119] Some additional Raman spectra assignments for carbon species features are given in Supporting Information Table S1.

https://dx.doi.org/10.1021/acscatal.0c01851
ACS Catal. 2020, 10, 9837−9855

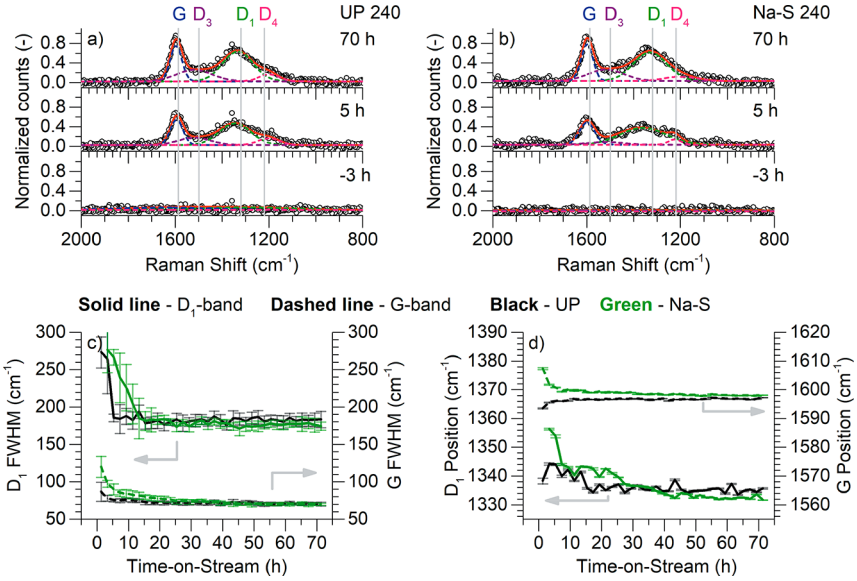

Figure 12. Peak fitting of the in situ collected Raman spectra of the 240 catalysts during a 72 h Fischer−Tropsch synthesis (FTS). The measured Raman spectra at −3, 5, and 70 h time-on-stream (ToS) with fitted G, D_1, D_3, and D_4 peaks for (a) UP 240 and (b) Na−S 240 (Fe(−Na−S)/α-Al_2O_3) catalysts. Vertical gray lines mark the corresponding nominal Raman band positions, fitted peaks are indicated by their colored letters, and the cumulative fit is in red. The peak D_1- and G-band widths over 72 h ToS are in (e) and positions are in (d) for UP and Na−S 240 catalysts.

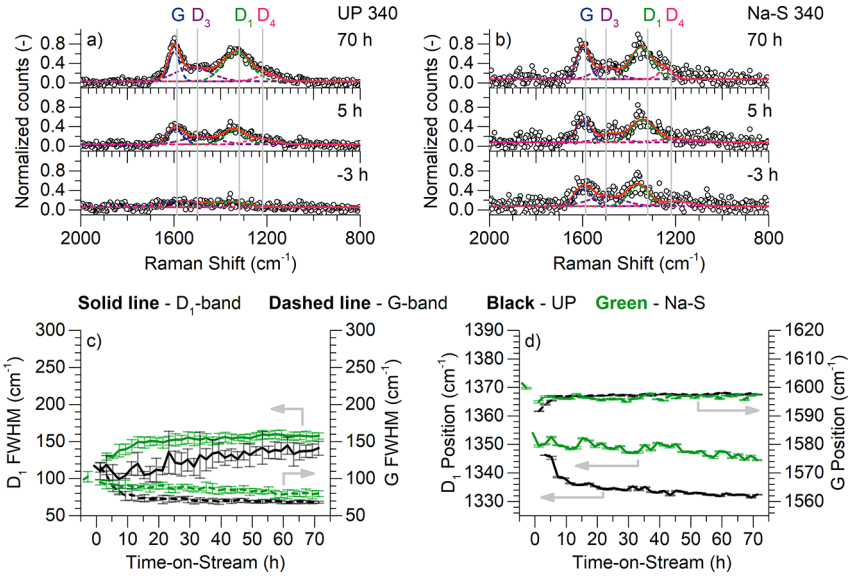

Figure 13. Peak fitting of the in situ collected Raman spectra of the 340 catalysts during a 72 h Fischer−Tropsch synthesis (FTS). The measured Raman spectra at −3, 5, and 70 h time-on-stream (ToS) with fitted G, D_1, D_3, and D_4 peaks for (a) UP 340 and (b) Na−S 340 (Fe(−Na−S)/α-Al_2O_3) catalysts. Vertical gray lines mark the corresponding nominal Raman band positions, fitted peaks are indicated by their colored letters, and the cumulative fit is in red. The peak D_1- and G-band widths over 72 h ToS are in (e) and positions are in (d) for UP and Na−S 340 catalysts.

By fitting the separate D_{1-4}- (and G-) band positions in the in situ Raman spectra with individual peaks, additional information should in principle be obtained. Our group has applied this approach earlier in operando experiments to study the formation of carbon species.[79−81] For each of the in situ Raman spectra, multiple peaks were fitted: one peak for G-band at ∼1590 cm^{-1} and three peaks to correspond to the D_1 (∼1320 cm^{-1}), D_3 (∼1500 cm^{-1}) and D_4 (∼1220 cm^{-1}) positions. It was not possible to fit a peak for the D_2 (∼1620 cm^{-1}) position. Lack of the sub-band peak for the D_2 position can be taken as indication of the presence of a poorly ordered graphite structure.[81]

Moreover, the fitted peak relative area or width errors for the D_3 and D_4 peaks were only occasionally below the set filtering condition of 40%. Therefore, no usable quantitative data could be collected for the D_3 or D_4 peaks. Therefore, in the following, the discussion is focused on the information collected from the fitted D_1- and G-bands, akin to what has been done earlier by our group.[79,81] In principle, the D_1- and G-bands provide sufficient information to identify the carbon species.[119]

The general trends for the shifts in the D_1- and G-band peak positions show similarities between the different FTS reaction runs, as illustrated in Figures 11−14. More specifically, it can be observed that (i) G-band positions start (∼0 h ToS) at >1600 cm^{-1} and shift $\lesssim$1600 cm^{-1}, (ii) D_1-band positions start at $\gtrsim$1350 cm^{-1} while shifting toward ∼1330 cm^{-1} by the time when ∼70 h ToS in the FTS reaction is reached. The Na−S

https://dx.doi.org/10.1021/acscatal.0c01851
ACS Catal. 2020, 10, 9837−9855

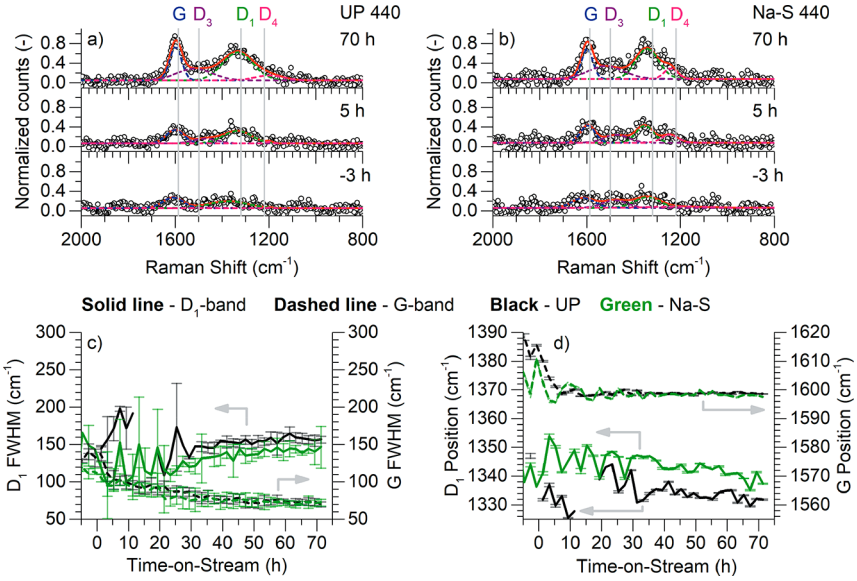

Figure 14. Peak fitting of the in situ collected Raman spectra of the 440 catalysts during a 72 h Fischer−Tropsch synthesis (FTS). The measured Raman spectra at −3, 5, and 70 h time-on-stream (ToS) with fitted G, D_1, D_3, and D_4 peaks for (a) UP 440 and (b) Na−S 440 (Fe(−Na−S)/α-Al_2O_3) catalysts. Vertical gray lines mark the corresponding nominal Raman band positions, fitted peaks are indicated by their colored letters, and the cumulative fit is in red. The peak D_1- and G-band widths over 72 h ToS are in (e) and positions are in (d) for UP and Na−S 440 catalysts.

promotion tends to (iii) increase the initial (~0 h ToS) G-band positions toward $\gtrsim$1600 cm^{-1}.

The initial, high (>1600 cm^{-1}) G-band Raman shifts are due to olefinic, chain-like carbon species with C sp^2 and (tetrahedral) C sp^3 amorphous carbon structures.[65,123] The high ($\gtrsim$ 1350 cm^{-1}) initial position for the D_1-band originates from the presence of amorphous carbon.[64] For both the D_1- and G-bands, the shifts toward lower wavenumbers during FTS (i.e., D_1-band → ~1330 cm^{-1} and G-band → ~1600 cm^{-1}) signify a transition toward an increasing C sp^2 content in relation to C sp^3. Also, more cyclic, rather than chain-like, carbon species form.[65]

The general trends in the D_1- and G-band peak widths (fwhm) evolution also suggest increasing carbon species ordering processes during FTS (Figures 11c−14c). Decreasing D_1- and G-band peak widths have been associated with increasing graphitization and ordering of the carbon species.[79,81]

The G-band widths decrease from an initial >100 cm^{-1} at ~0−10 h ToS toward 70−80 cm^{-1} at ~70 h ToS for all of the studied catalysts (Figures 11c−14c). This G-band width decrease can therefore be associated with a carbon species *ordering* processes during FTS.

For the D_1-band width evolution, the situation is mixed. For the UP and Na−S H_2 and 240 catalysts, the D_1-band widths decrease (from $\gtrsim$200 cm^{-1} to ~160−180 cm^{-1}) (Figures 11c and 12c), while for the UP and Na−S 340 and 440 catalysts, the D_1-band width increases (from ~100 to ~140−160 cm^{-1}) during FTS (Figures 13c and 14c). The decrease of the D_1-band width is associated with the carbon species ordering process.[79,81] The UP and Na−S 340 and 440 catalysts have initial carbon deposits from the CO carburization process. Also for these catalysts, the initial I(D)/I(G) ratios are higher, which is a sign of the increased initial presence of cyclic sixfold ordered carbon rings with C sp^2. Thus, the D_1-band width increase for the UP and Na−S 340 and 440 catalysts can be explained by the formation of cyclic C sp^2, non-sixfold cyclic carbon structures during FTS.[65] This is in line with the previous discussion on the I(D)/I(G) ratios for the UP and Na−S 340 and 440 catalyst materials.

Summarizing, it was found that the carbon species evolve from tetrahedral C sp^3 with C sp^2 in chain-like structured amorphous carbon species toward carbon materials with varying cyclic *but non-sixfold* order with features <7 nm in diameter. The trend of increasing ordering of the carbon species is in line with previous studies for carbon deposits formation during FTS.[51]

Comparison of the Raman Spectra to Those of Carbon Reference Materials. Further identification of the carbon species formed during FTS can be done by comparing the in situ collected Raman spectra at ~70 h ToS to (ex situ) measured carbon reference materials of graphite, carbon nanotubes (CNT), carbon nanofibers (CNF) and activated carbon (AC).

Saturated and unsaturated long-chained hydrocarbons, i.e., waxes, can also give observable Raman spectra[123] and can be produced in the FTS reaction. However, the collected Raman spectra do not show any particular resemblance to Raman spectra from wax samples (Figure S5).[123] Furthermore, an Fe-based FTS reaction at ~340 °C produces only a low amount of >C_{20} hydrocarbons,[124] while hydrocarbons with <C_{20} boil at ~340 °C.[125] Thus, it is unlikely that any condensed hydrocarbon wax species contribute in any significant manner to the collected Raman spectra.

As an example, in Figure 15, ex situ collected Raman spectra for some carbon reference materials are compared to the in situ collected Raman spectrum for the UP 340 catalyst at ~70 h ToS. The other measured catalysts gave comparable Raman spectra to the UP 340 catalyst at ~70 h ToS (Figures 11a−14a and 11b−14b). The in situ measured median values, at ~70 h ToS, for the D_1- and G-band peak positions, related peak widths as fwhms, and I(D)/I(G) ratios are given in Table 2 with the corresponding values for the carbon reference materials. By comparing the in situ collected Raman spectrum for the UP 340 catalyst, the most comparable carbon reference spectrum is the one of CNF (Figure 15). Both the D_1-band position and I(D)/I(G) ratio are very similar to the reference CNF material. However, the G-band position is at a higher wavenumber

https://dx.doi.org/10.1021/acscatal.0c01851
ACS Catal. 2020, 10, 9837−9855

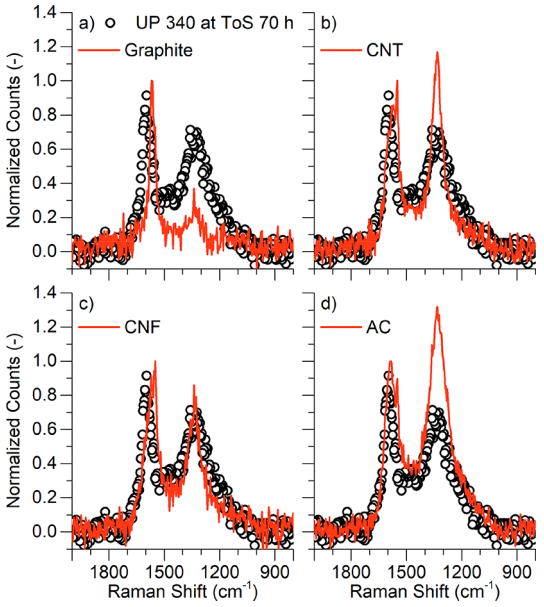

Figure 15. Comparison of in situ collected Raman spectrum of UP 340 (Fe/α-Al_2O_3) catalyst material at ~70 h time-on-stream (ToS) of Fischer–Tropsch synthesis (FTS) with ex situ measured carbon reference materials. Comparison of the Raman spectrum obtained on the catalyst material to (a) graphite, (b) a carbon nanotube (CNT), (c) carbon nanofiber (CNF), and (d) activated carbon (AC) carbon reference materials.

(~1598 versus ~1571 cm^{-1}), and the D_1-band width is also wider in the measured spectrum for the catalyst than for the reference CNF material. The G-band position is more akin to the G-band position with that of the AC reference carbon material (Figure 15).

The higher width of the measured D_1-band can be explained by a wider variety of carbon ring sizes, while the G-band shift toward a higher wavenumber would suggest the increased presence of C sp^2 in chain-like carbon species or clustering,[65] than is present in the reference CNF material. For the catalyst materials, Na–S 340 and Na–S 440 show in addition an increase in their D_1-band intensities in comparison to the rest of the catalysts at ~70 h ToS (Figures 13c and 14c). The D_1-band intensity increase, i.e., the increase in the $I(D)/I(G)$ ratio, is due to the increased presence of clustered cyclic sixfold C sp^2 carbon species.[65]

In summary on the discussion on type of carbon species formed and their evolution, it can be stated that the carbon species formed during the FTS reaction resemble most closely to those of the CNF reference material. With added Na–S promotion in comparison to the respective UP catalysts: (i) for H_2 and 240 catalysts, the carbon species evolution starts with more C sp^2 in chain-like species; (ii) more of the clustered 6-fold cyclic carbon species for the 340 and 440 catalysts are present; and (iii) the Fe_3O_4 phases are reduced more efficiently by CO, removing the onset time for the appearance of the carbon species between the Na–S H_2 and UP H_2 catalysts. It is noteworthy to mention that CNF contains "graphite-like" planes in their fiber structure.[37,54] Thus, assigning a Fe-based FTS reaction catalyst's deactivation to be due to "graphitic" carbon overlayers over the active Fe carbides should be done with care and with clear distinction to the possible presence of CNF materials. CNF materials grow away from the catalyst surface,[35,126] which is a significantly different phenomena than a carbon overlayer formation over the Fe surface.[126]

Finally, the carbon species formed under CO carburization and under H_2/CO during the FTS reaction are different. No significant or only weak Raman D- and G-bands were observed for the initial carbon-containing UP and Na–S 340 and 440 catalysts at the beginning of the FTS reactions.[39] Rather, the D_1- and G-bands appear and grow during FTS (Figures 9c,d and 10c,d). As based on the observations in literature, under pure CO, encapsulating carbon species form, while in the presence of H_2/CO, growth of filamentous carbon takes place.[35,37,55,56,126,127] This is in agreement with the results, i.e., the initial carbon deposits due to the CO carburization are formed mostly with C sp^3 structures, which are Raman inactive with the used (532 nm) visible wavelength excitation laser.[65] The formation of CNF-like carbon species with Raman active C sp^2 structures takes place under the applied FTS conditions in the presence of H_2/CO,[37] explaining the rise of the in situ collected Raman spectra for the studied catalyst materials (Figures 5 and 6).

CONCLUSIONS

Different Fe carbides were prepared on supported Fe(–Na–S)/α-Al_2O_3 catalyst materials via CO carburization. These catalysts

Table 2. In Situ Raman Spectroscopy Derived Median D_1- and G-Band Values at ~70 h Time-on-Stream (ToS) of the Fischer–Tropsch Synthesis (FTS) Reaction Runs for the Studied UP and Na–S (Fe(–Na–S)/α-Al_2O_3) Catalyst Materials

catalyst		D_1-band		G-band		
		position (cm^{-1})	fwhm (cm^{-1})	position (cm^{-1})	fwhm (cm^{-1})	$I(D)/I(G)$ (–)
H_2	UP	1332 ± 1	162 ± 5	1599 ± 0	69 ± 3	0.76 ± 0.05
	Na–S	1346 ± 2	172 ± 7	1600 ± 0	67 ± 1	0.66 ± 0.06
240	UP	1334 ± 0	183 ± 9	1597 ± 0	71 ± 2	0.73 ± 0.05
	Na–S	1334 ± 0	176 ± 9	1598 ± 0	71 ± 2	0.72 ± 0.04
340	UP	1331 ± 0	157 ± 5	1598 ± 0	68 ± 2	0.77 ± 0.05
	Na–S	1346 ± 0	137 ± 9	1597 ± 0	79 ± 6	0.89 ± 0.11
440	UP	1332 ± 0	155 ± 8	1599 ± 0	73 ± 5	0.82 ± 0.07
	Na–S	1342 ± 0	140 ± 17	1599 ± 0	71 ± 4	0.85 ± 0.10
reference materials	graphite	1334	113	1565	39	0.37
	CNF	1338	111	1571	89	0.86
	AC	1328	143	1584	97	1.31
	CNT	1333	86	1576	91	1.36

[a]fwhm = full width at half maximum (of fitted peak), CNF = carbon nanofiber, AC = activated carbon, CNT = carbon nanotubes.

https://dx.doi.org/10.1021/acscatal.0c01851
ACS Catal. 2020, 10, 9837–9855

were studied under in situ conditions with a combined XRPD/Raman spectroscopy setup.

Out of the prepared Fe carbides, namely, ε-Fe_3C $P6_322$ (182), η-Fe_2C *Pnnm* (58), χ-Fe_5C_2 *C2/c* (15) (the Hägg carbide), and θ-Fe_3C *Pnma* (62) (cementite), the χ-Fe_5C_2 phase was the most stable under the applied FTS reaction temperature of 340 °C. Furthermore, the Na−S promotion altered the Fe oxides and carbide phases' properties in the following manner

(i) *stabilizing* the η-Fe_2C phase, *but only if* either ε-Fe_3C and/or η-Fe_2C phase was present in the initial catalyst;
(ii) *destabilizing* the θ-Fe_3C phase and aiding in its transition to χ-Fe_5C_2;
(iii) increasing the reducibility of Fe_3O_4 phase by (H_2:)CO;
(iv) inducing Fe crystallite growth for the Fe carbides within the $\lesssim$15 h ToS, with the exception of the θ-Fe3C phase, for which the crystallite diameters decreased.

In situ Raman observed carbon deposition did not correlate with the presence of any specific Fe carbide phase or carbide-to-carbide transitions. However, with H_2 reduced catalysts, the initial carbon deposition did not start before the Fe_3O_4 phase, a phase incapable of CO dissociation, and was reduced to Fe carbides. For catalysts with insignificant amounts of initial carbon deposits, i.e., H_2 reduced or <300 °C CO carburized catalysts, the intensities of the Raman D- and G-bands grew during the FTS reaction. Two growth periods can be discerned: (i) an initial fast ($\lesssim$10−15 h ToS) and (ii) a steady or lesser ($\gtrsim$15 h ToS) intensity growth. The initial fast growth period occurs regardless of possible Na−S promotion. However, after the steady growth period was reached, Na−S promotion induced a higher rate of growth of the Raman D- and G-band intensities (for the G-band $\approx 2.5 \pm 0.9$ faster) in comparison to unpromoted catalysts. For catalysts with carbon deposits from CO carburization ≥340 °C, the initial fast growth period was absent. Possibly, an initial nonisothermal bed operation could explain the initial fast D- and G-band intensity gain within $\lesssim$10−15 h ToS.

Furthermore, the carbon species formed during CO carburization were weakly/non-Raman active with the used 532 nm excitation laser and therefore mainly consisted of structures with C sp^3. During FTS, under H_2/CO, more ordered CNF-like phases with C sp^2 are formed, resulting in an increased Raman signal intensity. Furthermore, over the course of the FTS reaction, the carbon species evolved from amorphous carbon species, with structures containing both tetrahedral C sp^3 and C sp^2 in chain-like ordering, toward more ordered carbon materials with their structures containing C sp^2 in varying non-sixfold cyclic order. In comparison to the measured carbon reference materials, the Raman spectra of the catalysts collected at ∼70 h ToS compared best to a CNF reference material.

Na−S promotion affected the type of carbon species formed during FTS, namely by (i) increasing the initial C sp^2 content in chain-like carbon structures and (ii) increasing 6-fold cyclic carbon species in catalyst materials with the initial CO carburization ≥340 °C.

■ ASSOCIATED CONTENT

Supporting Information

The Supporting Information is available free of charge at https://pubs.acs.org/doi/10.1021/acscatal.0c01851.

Photos of used setup and reactor cell with indication of measured reactor cell temperature profile; R_{wp} values for the used R-QPA fits; R-QPA derived elemental Fe contents for the catalysts; comparison of Raman spectra measured at different reactor bed locations for selected catalysts; measured Raman spectra for hydrocarbon reference samples; additional table for Raman band assignments and their sources (PDF)

■ AUTHOR INFORMATION

Corresponding Author

Bert M. Weckhuysen − *Inorganic Chemistry and Catalysis Group, Debye Institute of Nanomaterial Science, Utrecht University, 3584 CG Utrecht, The Netherlands;* orcid.org/0000-0001-5245-1426; Phone: (+31) 030 253 4328; Email: b.m.weckhuysen@uu.nl

Authors

Pasi P. Paalanen − *Inorganic Chemistry and Catalysis Group, Debye Institute of Nanomaterial Science, Utrecht University, 3584 CG Utrecht, The Netherlands*

Sophie H. van Vreeswijk − *Inorganic Chemistry and Catalysis Group, Debye Institute of Nanomaterial Science, Utrecht University, 3584 CG Utrecht, The Netherlands*

Complete contact information is available at: https://pubs.acs.org/10.1021/acscatal.0c01851

Notes

The authors declare no competing financial interest.

■ ACKNOWLEDGMENTS

This research received funding from the Dutch Research Council (NWO) in the framework of the TASC Technology Area "Syngas, a Switch to Flexible New feedstock for the Chemical Industry (TA-Syngas)". Dow Chemicals and Johnson-Matthey are also acknowledged for their funding. J. P. Falkenhagen (Utrecht University, UU) is thanked for his technical expertise and for providing design solutions for the in situ XRPD/Raman spectroscopy setup. O. Kerkenaar, P. Wijten, A. van der Eerden, H. Schaink, and R. van Zwienen (UU) are acknowledged for the design contributions and practical realization of the in situ XRPD/Raman spectroscopy setup.

■ REFERENCES

(1) Mittasch, A.; Schneider, C. Producing Compounds Containing Carbon and Hydrogen. US1201850 A, 1916.
(2) Dry, M. E. The Fischer−Tropsch Synthesis. In *Catalysis - Science and Technology*; Anderson, J. R., Boudart, M., Eds.; Springer-Verlag: Berlin, **1981**; Vol. *1*, pp 159−256.
(3) Muleja, A. A.; Gorimbo, J.; Masuku, C. M. Effect of Co-Feeding Inorganic and Organic Molecules in the Fe and Co Catalyzed Fischer−Tropsch Synthesis: A Review. *Catalysts* **2019**, *9* (9), 746.
(4) Dry, M. E. FT Catalysts. *Stud. Surf. Sci. Catal.* **2004**, *152*, 533−600.
(5) Dictor, R.; Bell, A. T. Fischer−Tropsch Synthesis over Reduced and Unreduced Iron Oxide Catalysts. *J. Catal.* **1986**, *97* (1), 121−136.
(6) Todic, B.; Nowicki, L.; Nikacevic, N.; Bukur, D. B. Fischer−Tropsch Synthesis Product Selectivity over an Industrial Iron-Based Catalyst: Effect of Process Conditions. *Catal. Today* **2016**, *261*, 28−39.
(7) van der Laan, G. P.; Beenackers, A. A. C. M. Kinetics and Selectivity of the Fischer−Tropsch Synthesis: A Literature Review. *Catal. Rev.: Sci. Eng.* **1999**, *41* (3−4), 255−318.
(8) dos Santos, R. G.; Alencar, A. C. Biomass-Derived Syngas Production via Gasification Process and Its Catalytic Conversion into Fuels by Fischer−Tropsch Synthesis: A Review. *Int. J. Hydrogen Energy* **2020**, *45*, 18114.

(9) Kirchner, J.; Baysal, Z.; Kureti, S. Activity and Structural Changes of Fe-based Catalysts during CO_2 Hydrogenation towards CH_4 − A Mini Review. *ChemCatChem* **2020**, *12* (4), 981−988.
(10) Mahmoudi, H.; Mahmoudi, M.; Doustdar, O.; Jahangiri, H.; Tsolakis, A.; Gu, S.; Lech Wyszynski, M. A Review of Fischer−Tropsch Synthesis Process, Mechanism, Surface Chemistry and Catalyst Formulation. *Biofuels Eng.* **2017**, *2* (1), 11−31.
(11) Molino, A.; Larocca, V.; Chianese, S.; Musmarra, D. Biofuels Production by Biomass Gasification: A Review. *Energies* **2018**, *11* (4), 811.
(12) Torres Galvis, H. M.; de Jong, K. P. Catalysts for Production of Lower Olefins from Synthesis Gas: A Review. *ACS Catal.* **2013**, *3* (9), 2130−2149.
(13) Torres Galvis, H. M.; Bitter, J. H.; Khare, C. B.; Ruitenbeek, M.; Dugulan, A. I.; de Jong, K. P. Supported Iron Nanoparticles as Catalysts for Sustainable Production of Lower Olefins. *Science* **2012**, *335* (6070), 835−838.
(14) Myddleton, W. W. Improvements Relating to the Catalytic Synthesis of Hydrocarbon Oils from Gaseous Mixtures of Carbon Monoxide and Hydrogen. GB509325 A, 1939.
(15) Torres Galvis, H. M.; Bitter, J. H.; Davidian, T.; Ruitenbeek, M.; Dugulan, A. I.; de Jong, K. P. Iron Particle Size Effects for Direct Production of Lower Olefins from Synthesis Gas. *J. Am. Chem. Soc.* **2012**, *134* (39), 16207−16215.
(16) Torres Galvis, H. M.; Koeken, A. C. J.; Bitter, J. H.; Davidian, T.; Ruitenbeek, M.; Dugulan, A. I.; De Jong, K. P. Effect of Precursor on the Catalytic Performance of Supported Iron Catalysts for the Fischer−Tropsch Synthesis of Lower Olefins. *Catal. Today* **2013**, *215*, 95−102.
(17) Torres Galvis, H. M.; Koeken, A. C. J.; Bitter, J. H.; Davidian, T.; Ruitenbeek, M.; Dugulan, A. I.; de Jong, K. P. Effects of Sodium and Sulfur on Catalytic Performance of Supported Iron Catalysts for the Fischer−Tropsch Synthesis of Lower Olefins. *J. Catal.* **2013**, *303*, 22−30.
(18) Botes, G. F.; Bromfield, T. C.; Coetzer, R. L. J.; Crous, R.; Gibson, P.; Ferreira, A. C. Development of a Chemical Selective Iron Fischer−Tropsch Catalyst. *Catal. Today* **2016**, *275*, 40−48.
(19) Xie, J.; Yang, J.; Dugulan, A. I.; Holmen, A.; Chen, D.; De Jong, K. P.; Louwerse, M. J. Size and Promoter Effects in Supported Iron Fischer−Tropsch Catalysts: Insights from Experiment and Theory. *ACS Catal.* **2016**, *6* (5), 3147−3157.
(20) Xie, J.; Torres Galvis, H. M.; Koeken, A. C. J.; Kirilin, A.; Dugulan, A. I.; Ruitenbeek, M.; de Jong, K. P. Size and Promoter Effects on Stability of Carbon-Nanofiber-Supported Iron-Based Fischer−Tropsch Catalysts. *ACS Catal.* **2016**, *6* (6), 4017−4024.
(21) Crous, R.; Bromfield, T. C.; Booyens, S. Olefin Selective FT Catalyst Composition and Preparation Thereof. WO2010066386 A1, 2010.
(22) Johnson, J. Y. Improvements in the Manufacture and Production of Unsaturated Hydrocarbons of Low Boiling Point. GB322284 A, 1929.
(23) Dry, M. E.; Shingles, T.; van H. Botha, C. S. Factors Influencing the Formation of Carbon on Iron Fischer−Tropsch Catalysts I. The Influence of Promoters. *J. Catal.* **1970**, *17* (3), 341−346.
(24) Dry, M. E.; Shingles, T.; Boshoff, L. J.; van H. Botha, C. S. Factors Influencing the Formation of Carbon on Iron Fischer−Tropsch Catalysts. II. The Effect of Temperature and of Gases and Vapors Present during Fischer−Tropsch Synthesis. *J. Catal.* **1970**, *17* (3), 347−354.
(25) Cohn, E. M.; Bean, E. H.; Mentser, M.; Hofer, L. J. E.; Pontello, A.; Peebles, W. C.; Jack, K. H. The Carburization of Iron Oxide with Carbon Monoxide: Modifications of Hägg Iron Carbide. *J. Appl. Chem.* **1955**, *5* (8), 418−425.
(26) Bartholomew, C. H. Mechanisms of Catalyst Deactivation. *Appl. Catal., A* **2001**, *212* (1−2), 17−60.
(27) Niemantsverdriet, J. W.; van der Kraan, A. M. On the Time-Dependent Behavior of Iron Catalysts in Fischer−Tropsch Synthesis. *J. Catal.* **1981**, *72* (2), 385−388.
(28) Dry, M. E. The Fischer−Tropsch Process: 1950−2000. *Catal. Today* **2002**, *71* (3−4), 227−241.
(29) Shultz, J. F.; Hall, W. K.; Seligman, B.; Anderson, R. B. Studies of the Fischer−Tropsch Synthesis. XIV. Hägg Carbide as Catalysts. *J. Am. Chem. Soc.* **1955**, *77* (1950), 213−221.
(30) Steynberg, A. P.; Espinoza, R. L.; Jager, B.; Vosloo, A. C. High Temperature Fischer−Tropsch Synthesis in Commercial Practice. *Appl. Catal., A* **1999**, *186* (1−2), 41−54.
(31) Benziger, J.; Madix, R. J. The Effects of Carbon, Oxygen, Sulfur and Potassium Adlayers on CO and H_2 Adsorption on Fe(100). *Surf. Sci.* **1980**, *94* (1), 119−153.
(32) Le Caër, G.; Dubois, J. M.; Pijolat, M.; Perrichon, V.; Bussière, P. Characterization by Moessbauer Spectroscopy of Iron Carbides Formed by Fischer−Tropsch Synthesis. *J. Phys. Chem.* **1982**, *86* (24), 4799−4808.
(33) de Smit, E.; Beale, A. M.; Nikitenko, S.; Weckhuysen, B. M. Local and Long Range Order in Promoted Iron-Based Fischer−Tropsch Catalysts: A Combined in Situ X-Ray Absorption Spectroscopy/Wide Angle X-Ray Scattering Study. *J. Catal.* **2009**, *262* (2), 244−256.
(34) de Smit, E.; Cinquini, F.; Beale, A. M.; Safonova, O. V.; van Beek, W.; Sautet, P.; Weckhuysen, B. M. Stability and Reactivity of E-χ-θ Iron Carbide Catalyst Phases in Fischer−Tropsch Synthesis: Controlling μ_C. *J. Am. Chem. Soc.* **2010**, *132* (42), 14928−14941.
(35) Mazzucco, S.; Wang, Y.; Tanase, M.; Picher, M.; Li, K.; Wu, Z.; Irle, S.; Sharma, R. Direct Evidence of Active and Inactive Phases of Fe Catalyst Nanoparticles for Carbon Nanotube Formation. *J. Catal.* **2014**, *319*, 54−60.
(36) Jung, H.; Thomson, W. J. Dynamic X-Ray Diffraction Study of an Unsupported Iron Catalyst in Fischer−Tropsch Synthesis. *J. Catal.* **1992**, *134* (2), 654−667.
(37) Kock, A. J. H. M.; de Bokx, P. K.; Boellaard, E.; Klop, W.; Geus, J. W. The Formation of Filamentous Carbon on Iron and Nickel Catalysts II. Mechanism. *J. Catal.* **1985**, *96* (2), 468−480.
(38) Eliason, S. A.; Bartholomew, C. H. Reaction and Deactivation Kinetics for Fischer−Tropsch Synthesis on Unpromoted and Potassium-Promoted Iron Catalysts. *Appl. Catal., A* **1999**, *186* (1−2), 229−243.
(39) Paalanen, P. P.; van Vreeswijk, S.; Dugulan, A. I.; Weckhuysen, B. M. Identification of Iron Carbides in Fe(-Na-S)/α-Al_2O_3 Fischer−Tropsch Synthesis Catalysts with X-ray Powder Diffractometry and Mössbauer Absorption Spectroscopy. *ChemCatChem* **2020**, DOI: 10.1002/cctc.202000707.
(40) Schneider, A.; Inden, G. Carbon Diffusion in Cementite (Fe_3C) and Hägg Carbide (Fe_5C_2). *CALPHAD: Comput. Coupling Phase Diagrams Thermochem.* **2007**, *31* (1), 141−147.
(41) Moszyński, D.; Grabke, H. J.; Schneider, A. Effect of Sulphur on the Formation of Graphite at the Surface of Carburized Iron. *Surf. Interface Anal.* **2002**, *34* (1), 380−383.
(42) Olsson, R. G.; Turkdogan, E. T. Catalytic Effect of Iron on Decomposition of Carbon Monoxide: II. Effect of Additions of H_2, H_2O, CO_2, SO_2 and H_2S. *Metall. Trans.* **1974**, *5* (1), 21.
(43) Arabczyk, W.; Moszyński, D.; Narkiewicz, U.; Pelka, R.; Podsiadły, M. Poisoning of Iron Catalyst by Sulfur. *Catal. Today* **2007**, *124* (1−2), 43−48.
(44) Berry, T. F.; Ames, R. N.; Snow, R. B. Influence of Impurities and Role of Iron Carbides in Deposition of Carbon from Carbon Monoxide. *J. Am. Ceram. Soc.* **1956**, *39* (9), 308−318.
(45) Xu, J.-D.; Chang, Z.-Y.; Zhu, K.-T.; Weng, X.-F.; Weng, W.-Z.; Zheng, Y.-P.; Huang, C.-J.; Wan, H.-L. Effect of Sulfur on α-Al_2O_3-Supported Iron Catalyst for Fischer−Tropsch Synthesis. *Appl. Catal., A* **2016**, *514*, 103−113.
(46) Zhou, X.; Ji, J.; Wang, D.; Duan, X.; Qian, G.; Chen, D.; Zhou, X. Hierarchical Structured α-Al2O3 Supported S-Promoted Fe Catalysts for Direct Conversion of Syngas to Lower Olefins. *Chem. Commun.* **2015**, *51* (42), 8853−8856.
(47) Dalla Betta, R. A.; Piken, A. G.; Shelef, M. Heterogeneous Methanation: Steady-State Rate of CO Hydrogenation on Supported Ruthenium, Nickel and Rhenium. *J. Catal.* **1975**, *40* (2), 173−183.
(48) van Dijk, W. L.; Niemantsverdriet, J. W.; van dar Kraan, A. M.; van der Baan, H. S. Effects of Manganese Oxide and Sulphate on the

Olefin Selectivity of Iron Catalysts in the Fischer−Tropsch Reaction. *Appl. Catal.* **1982**, *2* (4−5), 273−288.
(49) Madon, R. J.; Seaw, H. Effect of Sulfur on the Fischer−Tropsch Synthesis. *Catal. Rev.: Sci. Eng.* **1977**, *15* (1), 69−106.
(50) Herranz, T.; Rojas, S.; Pérez-Alonso, F. J.; Ojeda, M.; Terreros, P.; Fierro, J. L. G. Genesis of Iron Carbides and Their Role in the Synthesis of Hydrocarbons from Synthesis Gas. *J. Catal.* **2006**, *243* (1), 199−211.
(51) Xu, J.; Bartholomew, C. H. Temperature-Programmed Hydrogenation (TPH) and in Situ Mössbauer Spectroscopy Studies of Carbonaceous Species on Silica-Supported Iron Fischer−Tropsch Catalysts. *J. Phys. Chem. B* **2005**, *109* (6), 2392−2403.
(52) Hamilton, N. G.; Warringham, R.; Silverwood, I. P.; Kapitán, J.; Hecht, L.; Webb, P. B.; Tooze, R. P.; Zhou, W.; Frost, C. D.; Parker, S. F.; et al. The Application of Inelastic Neutron Scattering to Investigate CO Hydrogenation over an Iron Fischer−Tropsch Synthesis Catalyst. *J. Catal.* **2014**, *312*, 221−231.
(53) Ning, W.; Koizumi, N.; Chang, H.; Mochizuki, T.; Itoh, T.; Yamada, M. Phase Transformation of Unpromoted and Promoted Fe Catalysts and the Formation of Carbonaceous Compounds during Fischer−Tropsch Synthesis Reaction. *Appl. Catal., A* **2006**, *312* (1−2), 35−44.
(54) Nolan, P. E.; Lynch, D. C.; Cutler, A. H. Carbon Deposition and Hydrocarbon Formation on Group VIII Metal Catalysts. *J. Phys. Chem. B* **1998**, *102* (21), 4165−4175.
(55) Boellaard, E.; de Bokx, P. K.; Kock, A. J. H. M.; Geus, J. W. The Formation of Filamentous Carbon on Iron and Nickel Catalysts III. Morphology. *J. Catal.* **1985**, *96* (2), 481−490.
(56) de Bokx, P. K.; Kock, A. J. H. M.; Boellaard, E.; Klop, W.; Geus, J. W. The Formation of Filamentous Carbon on Iron and Nickel Catalysts. I. Thermodynamics. *J. Catal.* **1985**, *96* (2), 454−467.
(57) Bukur, D. B.; Okabe, K.; Rosynek, M. P.; Li, C. P.; Wang, D. J.; Rao, K. R. P. M.; Huffman, G. P. Activation Studies with a Precipitated Iron Catalyst for Fischer−Tropsch Synthesis. I. Characterization Studies. *J. Catal.* **1995**, *155*, 353−365.
(58) McCartney, J. T.; Hofer, L. J. E.; Seligman, B.; Lecky, J. A.; Peebles, W. C.; Anderson, R. B. Electron and X-Ray Diffraction Studies of Iron Fischer−Tropsch Catalysts. *J. Phys. Chem.* **1953**, *57* (7), 730−736.
(59) Datye, A. K.; Jin, Y.; Mansker, L. D.; Motjope, R. T.; Dlamini, T. H.; Coville, N. J. The Nature of the Active Phase in Iron Fischer−Tropsch Catalysts. *Stud. Surf. Sci. Catal.* **2000**, *130*, 1139−1144.
(60) O'Brien, R. J.; Xu, L.; Milburn, D. R.; Li, Y.-X.; Klabunde, K. J.; Davis, B. H. Fischer−Tropsch Synthesis: Impact of Potassium and Zirconium Promoters on the Activity and Structure of an Ultrafine Iron Oxide Catalyst. *Top. Catal.* **1995**, *2* (1−4), 1−15.
(61) Mansker, L. D.; Jin, Y.; Bukur, D. B.; Datye, A. K. Characterization of Slurry Phase Iron Catalysts for Fischer−Tropsch Synthesis. *Appl. Catal., A* **1999**, *186* (1−2), 277−296.
(62) Wang, Y.; Alsmeyer, D. C.; McCreery, R. L. Raman Spectroscopy of Carbon Materials: Structural Basis of Observed Spectra. *Chem. Mater.* **1990**, *2* (5), 557−563.
(63) Wang, Y.; Serrano, S.; Santiago-Avilés, J. J. *Synth. Met.* **2003**, *138*, 423−427.
(64) Shimodaira, N.; Masui, A. Raman Spectroscopic Investigations of Activated Carbon Materials. *J. Appl. Phys.* **2002**, *92* (2), 902−909.
(65) Ferrari, A. C.; Robertson, J. Interpretation of Raman Spectra of Disordered and Amorphous Carbon. *Phys. Rev. B: Condens. Matter Mater. Phys.* **2000**, *61* (20), 14095−14107.
(66) Escribano, R.; Sloan, J. J.; Siddique, N.; Sze, N.; Dudev, T. Raman Spectroscopy of Carbon-Containing Particles. *Vib. Spectrosc.* **2001**, *26* (2), 179−186.
(67) Cruz, M. G. A.; Bastos-Neto, M.; Oliveira, A. C.; Filho, J. M.; Soares, J. M.; Rodríguez-Castellón, E.; Fernandes, F. A. N. On the Structural, Textural and Morphological Features of Fe-Based Catalysts Supported on Polystyrene Mesoporous Carbon for Fischer−Tropsch Synthesis. *Appl. Catal., A* **2015**, *495*, 72−83.
(68) Díaz, J. A.; Romero, A.; García-Minguillán, A. M.; Giroir-Fendler, A.; Valverde, J. L. Carbon Nanofibers and Nanospheres-Supported Bimetallic (Co and Fe) Catalysts for the Fischer−Tropsch Synthesis. *Fuel Process. Technol.* **2015**, *138*, 455−462.
(69) Yang, Z.; Luo, M.; Liu, Q.; Shi, B. In Situ XRD and Raman Investigation of the Activation Process over K−Cu−Fe/SiO2 Catalyst for Fischer−Tropsch Synthesis Reaction. *Catal. Lett.* **2020**, *150* (8), 2437.
(70) Zhang, Z.; Zhang, J.; Wang, X.; Si, R.; Xu, J.; Han, Y. F. Promotional Effects of Multiwalled Carbon Nanotubes on Iron Catalysts for Fischer−Tropsch to Olefins. *J. Catal.* **2018**, *365*, 71−85.
(71) Duan, X.; Wang, D.; Qian, G.; Walmsley, J. C.; Holmen, A.; Chen, D.; Zhou, X. Fabrication of K-Promoted Iron/Carbon Nanotubes Composite Catalysts for the Fischer−Tropsch Synthesis of Lower Olefins. *J. Energy Chem.* **2016**, *25* (2), 311−317.
(72) Li, J.; He, Y.; Tan, L.; Zhang, P.; Peng, X.; Oruganti, A.; Yang, G.; Abe, H.; Wang, Y.; Tsubaki, N. Integrated Tuneable Synthesis of Liquid Fuels via Fischer−Tropsch Technology. *Nat. Catal.* **2018**, *1* (10), 787−793.
(73) Ma, Z.; Zhou, C.; Wang, D.; Wang, Y.; He, W.; Tan, Y.; Liu, Q. Co-Precipitated Fe-Zr Catalysts for the Fischer−Tropsch Synthesis of Lower Olefins ($C_2 \sim C_4$): Synergistic Effects of Fe and Zr. *J. Catal.* **2019**, *378*, 209−219.
(74) Nasser, A. H.; Guo, L.; Elnaggar, H.; Wang, Y.; Guo, X.; Abdelmoneim, A.; Tsubaki, N. Mn-Fe Nanoparticles on a Reduced Graphene Oxide Catalyst for Enhanced Olefin Production from Syngas in a Slurry Reactor. *RSC Adv.* **2018**, *8* (27), 14854−14863.
(75) Pérez, S.; Mondragón, F.; Moreno, A. Iron Ore as Precursor for Preparation of Highly Active χ-Fe_5C_2 Core-Shell Catalyst for Fischer−Tropsch Synthesis. *Appl. Catal., A* **2019**, *587* (April), 117264.
(76) Wang, H.; Huang, S.; Wang, J.; Zhao, Q.; Wang, Y.; Wang, Y.; Ma, X. Effect of Ca Promoter on the Structure and Catalytic Behavior of FeK/Al2O3 Catalyst in Fischer−Tropsch Synthesis. *ChemCatChem* **2019**, *11* (14), 3220−3226.
(77) Wei, Y.; Luo, D.; Zhang, C.; Liu, J.; He, Y.; Wen, X.; Yang, Y.; Li, Y. Precursor Controlled Synthesis of Graphene Oxide Supported Iron Catalysts for Fischer−Tropsch Synthesis. *Catal. Sci. Technol.* **2018**, *8* (11), 2883−2893.
(78) Yan, Q.; Street, J.; Yu, F. Synthesis of Carbon-Encapsulated Iron Nanoparticles from Wood Derived Sugars by Hydrothermal Carbonization (HTC) and Their Application to Convert Bio-Syngas into Liquid Hydrocarbons. *Biomass Bioenergy* **2015**, *83*, 85−95.
(79) Sattler, J. J. H. B.; Beale, A. M.; Weckhuysen, B. M. Operando Raman Spectroscopy Study on the Deactivation of Pt/Al_2O_3 and $Pt−Sn/Al_2O_3$ Propane Dehydrogenation Catalysts. *Phys. Chem. Chem. Phys.* **2013**, *15* (29), 12095.
(80) Sattler, J. J. H. B.; Mens, A. M.; Weckhuysen, B. M. Real-Time Quantitative Operando Raman Spectroscopy of a CrO_x/Al_2O_3 Propane Dehydrogenation Catalyst in a Pilot-Scale Reactor. *ChemCatChem* **2014**, *6* (11), 3139−3145.
(81) Cats, K. H.; Weckhuysen, B. M. Combined Operando X-Ray Diffraction/Raman Spectroscopy of Catalytic Solids in the Laboratory: The Co/TiO_2 Fischer−Tropsch Synthesis Catalyst Showcase. *ChemCatChem* **2016**, *8* (8), 1531−1542.
(82) Fischer, N.; Claeys, M. Phase Changes Studied under in Situ Conditions - A Novel Cell. *Catal. Today* **2016**, *275*, 149−154.
(83) Centre for Catalysis Research - University of Cape Town. iKey in-situ XRD Cell. http://www.catcentre.uct.ac.za/cat/ikey-products/xrd-cell (accessed Mar 26, 2020).
(84) Cape Catalytix. Laboratory and Research Equipment. https://capecatalytix.com (accessed May 10, 2020).
(85) Bare, S. R.; Yang, N.; Kelly, S. D.; Mickelson, G. E.; Modica, F. S. Design and Operation of a High Pressure Reaction Cell for in Situ X-Ray Absorption Spectroscopy. *Catal. Today* **2007**, *126* (1−2), 18−26.
(86) Fischer, N.; Claeys, M. In Situ Characterization of Fischer−Tropsch Catalysts: A Review. *J. Phys. D: Appl. Phys.* **2020**, *53* (29), 293001.
(87) Clausen, B. S.; Steffensen, F. B.; Villadsen, J.; Feidenhans'L, R.; Topsøe, H. In Situ Cell for Combined XRD and On-Line Catalysis Tests: Studies of Cu-Based Water Gas Shift and Methanol Catalysts. *J. Catal.* **1991**, *132* (2), 524−535.

https://dx.doi.org/10.1021/acscatal.0c01851
ACS Catal. 2020, 10, 9837−9855

(88) Wood, I. G.; Vočadlo, L.; Knight, K. S.; Dobson, D. P.; Marshall, W. G.; Price, G. D.; Brodholt, J. Thermal Expansion and Crystal Structure of Cementite, Fe_3C, between 4 and 600 K Determined by Time-of-Flight Neutron Powder Diffraction. *J. Appl. Crystallogr.* **2004**, *37* (1), 82−90.
(89) Sabine, T. M.; Hunter, B. A.; Sabine, W. R.; Ball, C. J. Analytical Expressions for the Transmission Factor and Peak Shift in Absorbing Cylindrical Specimens. *J. Appl. Crystallogr.* **1998**, *31* (1), 47−51.
(90) Paalanen, P. P.; Weckhuysen, B. M. Carbon Pathways, Sodium-Sulfur Promotion and Identification of Iron Carbides in Iron-Based Fischer−Tropsch Synthesis. *ChemCatChem* **2020**, DOI: 10.1002/cctc.202001208.
(91) Michel, F. M.; Ehm, L.; Antao, S. M.; Lee, P. L.; Chupas, P. J.; Liu, G.; Strongin, D. R.; Schoonen, M. A. A.; Phillips, B. L.; Parise, J. B. The Structure of Ferrihydrite, a Nanocrystalline Material. *Science* **2007**, *316* (5832), 1726−1729.
(92) Nagakura, S. Study of Metallic Carbides by Electron Diffraction Part III. Iron Carbides. *J. Phys. Soc. Jpn.* **1959**, *14* (2), 186−195.
(93) Amelse, J. A.; Grynkewich, G.; Butt, J. B.; Schwartz, L. H. Moessbauer Spectroscopic Study of Passivated Small Particles of Iron and Iron Carbide. *J. Phys. Chem.* **1981**, *85* (17), 2484−2488.
(94) Jiang, F.; Zhang, M.; Liu, B.; Xu, Y.; Liu, X. Insights into the Influence of Support and Potassium or Sulfur Promoter on Iron-Based Fischer−Tropsch Synthesis: Understanding the Control of Catalytic Activity, Selectivity to Lower Olefins, and Catalyst Deactivation. *Catal. Sci. Technol.* **2017**, *7* (5), 1245−1265.
(95) Raupp, G. B.; Delgass, W. N. Mössbauer Investigation of Supported Fe and FeNi Catalysts II. Carbides Formed by Fischer−Tropsch Synthesis. *J. Catal.* **1979**, *58* (3), 348−360.
(96) Tau, L. M.; Borcar, S.; Bianchi, D.; Bennett, C. O. Investigation of Supported Iron Fischer−Tropsch Synthesis Catalysts by Mössbauer Spectroscopy. *J. Catal.* **1984**, *87* (1), 36−54.
(97) du Plessis, H. E.; de Villiers, J. P. R.; Kruger, G. J.; Steuwer, A.; Brunelli, M. Rietveld and Pair Distribution Function Study of Hägg Carbide Using Synchrotron X-Ray Diffraction. *J. Synchrotron Radiat.* **2011**, *18* (2), 266−271.
(98) Hofer, L. J. E. *Nature of the Carbides of Iron*; National Institute for Occupational Safety and Health: Washington D.C., 1966.
(99) Riedel, T.; Schulz, H.; Schaub, G.; Jun, K.-W.; Hwang, J.-S.; Lee, K.-W. Fischer−Tropsch on Iron with H_2/CO and H_2/CO_2 as Synthesis Gases: The Episodes of Formation of the Fischer−Tropsch Regime and Construction of the Catalyst. *Top. Catal.* **2003**, *26* (1−4), 41−54.
(100) Berry, F. J.; Smith, M. R. A Mössbauer Investigation of Iron-Containing Catalysts Prepared at Low Temperatures and Active for Carbon Monoxide Hydrogenation. *J. Chem. Soc., Faraday Trans. 1* **1989**, *85* (2), 467−477.
(101) Ribeiro, M. C.; Jacobs, G.; Davis, B. H.; Cronauer, D. C.; Kropf, A. J.; Marshall, C. L. Fischer−Tropsch Synthesis: An In-Situ TPR-EXAFS/XANES Investigation of the Influence of Group I Alkali Promoters on the Local Atomic and Electronic Structure of Carburized Iron/Silica Catalysts. *J. Phys. Chem. C* **2010**, *114* (17), 7895−7903.
(102) Manes, M.; Damick, A. D.; Mentser, M.; Cohn, E. M.; Hofer, L. J. E. Hexagonal Iron Carbide as an Intermediate in the Carbiding of Iron Fischer—Tropsch Catalysts. *J. Am. Chem. Soc.* **1952**, *74* (24), 6207−6209.
(103) Boellaard, E.; van der Kraan, A. M.; Geus, J. W. Behaviour of a Cyanide-Derived Fe/Al_2O_3 Catalyst during Fischer−Tropsch Synthesis. *Appl. Catal., A* **1996**, *147* (1), 229−245.
(104) Pijolat, M.; Perrichon, V.; Bussière, P. Study of the Carburization of an Iron Catalyst during the Fischer−Tropsch Synthesis: Influence on Its Catalytic Activity. *J. Catal.* **1987**, *107* (1), 82−91.
(105) Butt, J. B. Carbide Phases on Iron-Based Fischer−Tropsch Synthesis Catalysts Part II: Some Reaction Studies. *Catal. Lett.* **1991**, *7* (1−4), 83−106.
(106) Pendyala, V. R. R.; Graham, U. M.; Jacobs, G.; Hamdeh, H. H.; Davis, B. H. Fischer−Tropsch Synthesis: Deactivation as a Function of Potassium Promoter Loading for Precipitated Iron Catalyst. *Catal. Lett.* **2014**, *144* (10), 1704−1716.
(107) An, X.; Wu, B.; Wan, H.-J.; Li, T.-Z.; Tao, Z.-C.; Xiang, H.-W.; Li, Y.-W. Comparative Study of Iron-Based Fischer−Tropsch Synthesis Catalyst Promoted with Potassium or Sodium. *Catal. Commun.* **2007**, *8* (12), 1957−1962.
(108) Shultz, J. F.; Abelson, M.; Shaw, L.; Anderson, R. B. Fischer−Tropsch Synthesis. Nitrides and Carbonitrides of Iron as Catalysts. *Ind. Eng. Chem.* **1957**, *49* (12), 2055−2060.
(109) Niewa, R.; Rau, D.; Wosylus, A.; Meier, K.; Hanfland, M.; Wessel, M.; Dronskowski, R.; Dzivenko, D. A.; Riedel, R.; Schwarz, U. High-Pressure, High-Temperature Single-Crystal Growth, Ab Initio Electronic Structure Calculations, and Equation of State of ε-Fe_3N_{1+x}. *Chem. Mater.* **2009**, *21* (2), 392−398.
(110) Leineweber, A.; Shang, S.; Liu, Z.-K.; Widenmeyer, M.; Niewa, R. Crystal Structure Determination of Hägg Carbide, χ-Fe_5C_2 by First-Principles Calculations and Rietveld Refinement. *Zeitschrift für Krist.* **2012**, *227* (4), 207−220.
(111) Jack, K. H. The Iron−Nitrogen System: The Crystal Structures of ε-Phase Iron Nitrides. *Acta Crystallogr.* **1952**, *5* (4), 404−411.
(112) Rechenbach, D.; Jacobs, H. Structure Determination of ζ-Fe_2N by Neutron and Synchrotron Powder Diffraction. *J. Alloys Compd.* **1996**, *235* (1), 15−22.
(113) Jacobs, H.; Rechenbach, D.; Zachwieja, U. Structure Determination of Γ'-Fe_4N and ϵ-Fe_3N. *J. Alloys Compd.* **1995**, *227* (1), 10−17.
(114) Nagakura, S.; Tanehashi, K. Electronic Structure of Iron Nitrides Studied by Electron Diffraction. II. ε-Fe_2N and ζ-Fe_2N. *J. Phys. Soc. Jpn.* **1968**, *25* (3), 840−846.
(115) O'Brien, R. J.; Xu, L.; Spicer, R. L.; Davis, B. H. Activation Study of Precipitated Iron Fischer−Tropsch Catalysts. *Energy Fuels* **1996**, *10* (4), 921−926.
(116) Shultz, J. F.; Abelson, M.; Stein, K. C.; Anderson, R. B. Studies of the Fischer−Tropsch Synthesis. XVIII. Influence of Catalyst Geometry on Synthesis on Iron Catalysts. *J. Phys. Chem.* **1959**, *63* (4), 496−500.
(117) Anderson, R. B.; Hofer, L. J. E.; Cohn, E. M.; Seligman, B. Studies of the Fischer—Tropsch Synthesis. IX. Phase Changes of Iron Catalysts in the Synthesis. *J. Am. Chem. Soc.* **1951**, *73* (3), 944−946.
(118) Matyi, R. J.; Schwartz, L. H.; Butt, J. B. Particle Size, Particle Size Distribution, and Related Measurements of Supported Metal Catalysts. *Catal. Rev.: Sci. Eng.* **1987**, *29* (1), 41−99.
(119) Sadezky, A.; Muckenhuber, H.; Grothe, H.; Niessner, R.; Pöschl, U. Raman Microspectroscopy of Soot and Related Carbonaceous Materials: Spectral Analysis and Structural Information. *Carbon* **2005**, *43* (8), 1731−1742.
(120) Ratnasamy, C.; Wagner, J. P. Water Gas Shift Catalysis. *Catal. Rev.: Sci. Eng.* **2009**, *51* (3), 325−440.
(121) Podgurski, H. H.; Kummer, J. T.; DeWitt, T. W.; Emmett, P. H. Preparation, Stability and Adsorptive Properties of the Carbides of Iron. *J. Am. Chem. Soc.* **1950**, *72* (12), 5382−5388.
(122) Sancier, K. M.; Isakson, W. E.; Wise, H. Carburization Studies of Iron Fischer−Tropsch Catalysts. *Adv. Chem. Ser.* **1979**, *178*, 129−145.
(123) Edwards, H. G. M.; Falk, M. J. P. Fourier-Transform Raman Spectroscopic Study of Unsaturated and Saturated Waxes. *Spectrochim. Acta, Part A* **1997**, *53* (14), 2685−2694.
(124) Maitlis, P. M., de Klerk, A., Eds. *Greener Fischer−Tropsch Processes for Fuels and Feedstocks*; Wiley-VCH: Weinheim, 2013.
(125) Yaws, C. L., Ed. *Thermophysical Properties of Chemicals and Hydrocarbons*, 1st ed.; Elsevier: Amsterdam, 2009.
(126) Nolan, P. E.; Lynch, D. C.; Cutler, A. H. Catalytic Disproportionation of CO in the Absence of Hydrogen: Encapsulating Shell Carbon Formation. *Carbon* **1994**, *32* (3), 477−483.
(127) Alstrup, I.; Tavares, M. T.; Bernardo, C. A.; Sørensen, O.; Rostrup-Nielsen, J. R. Carbon Formation on Nickel and Nickel-Copper Alloy Catalysts. *Mater. Corros.* **1998**, *49* (5), 367−372.

https://dx.doi.org/10.1021/acscatal.0c01851
ACS Catal. 2020, 10, 9837−9855